

Consistent Iron Abundances Derived from Neutral and Singly-Ionized Iron Lines  
in Ultraviolet and Optical Spectra of Six Warm Metal-Poor Stars\*

IAN U. ROEDERER,<sup>1,2</sup> CHRISTOPHER SNEDEN,<sup>3</sup> JAMES E. LAWLER,<sup>4</sup> JENNIFER S. SOBECK,<sup>5</sup> JOHN J. COWAN,<sup>6</sup> AND  
ANN MERCHANT BOESGAARD<sup>7</sup>

<sup>1</sup>*Department of Astronomy, University of Michigan, 1085 S. University Ave., Ann Arbor, MI 48109, USA*

<sup>2</sup>*Joint Institute for Nuclear Astrophysics - Center for the Evolution of the Elements (JINA-CEE), USA*

<sup>3</sup>*Department of Astronomy and McDonald Observatory, The University of Texas, Austin, TX 78712, USA*

<sup>4</sup>*Department of Physics, University of Wisconsin-Madison, Madison, WI 53706, USA*

<sup>5</sup>*Department of Astronomy, University of Washington, Seattle, WA 98195, USA*

<sup>6</sup>*Homer L. Dodge Department of Physics and Astronomy, University of Oklahoma, Norman, OK 73019, USA*

<sup>7</sup>*Institute for Astronomy, University of Hawai'i at Manoa, 2680 Woodlawn Drive, Honolulu, HI 96822, USA*

(Accepted for publication in the *Astrophysical Journal*)

ABSTRACT

Neutral Fe lines in metal-poor stars yield conflicting abundances depending on whether and how deviations from local thermodynamic equilibrium (LTE) are considered. We have collected new high resolution and high signal-to-noise ultraviolet (UV) spectra of three warm dwarf stars with  $[\text{Fe}/\text{H}] \approx -2.9$  with the Space Telescope Imaging Spectrograph on the *Hubble Space Telescope*. We locate archival UV spectra for three other warm dwarfs with  $[\text{Fe}/\text{H}] \approx -3.3$ ,  $-2.2$ , and  $-1.6$ , supplemented with optical spectra for all six stars. We calculate stellar parameters using methods that are largely independent of the spectra, adopting broadband photometry, color-temperature relations, *Gaia* parallaxes, and assumed masses. We use the LTE line analysis code MOOG to derive Fe abundances from hundreds of Fe I and Fe II lines with wavelengths from 2290 to 6430 Å. The  $[\text{Fe}/\text{H}]$  ratios derived separately from Fe I and Fe II lines agree in all six stars, with  $[\text{Fe II}/\text{H}] - [\text{Fe I}/\text{H}]$  ranging from  $+0.00 \pm 0.07$  to  $-0.12 \pm 0.09$  dex, when strong lines and Fe I lines with lower excitation potential  $< 1.2$  eV are excluded. This constrains the extent of any deviations from LTE that may occur within this parameter range. While our result confirms non-LTE calculations for some warm, metal-poor dwarfs, it may not be generalizable to more metal-poor dwarfs, where deviations from LTE are predicted to be larger. We also investigate trends of systematically lower abundances derived from Fe I lines in the Balmer continuum region ( $\approx 3100\text{--}3700$  Å), and we conclude that no proposed explanation for this effect can fully account for the observations presently available.

*Keywords:* stars: abundances — stars: atmospheres — stars: individual (BD+03°740, BD−13°3442, CD−33°1173, G 64-12, HD 19445, HD 84937, HD 94028) — stars: population II

Email: iur@umich.edu

\* Based on observations made with the NASA/ESA *Hubble Space Telescope*, obtained at the Space Telescope Science Institute (STScI), which is operated by the Association of Universities for Research in Astronomy, Inc. (AURA) under NASA contract NAS 5-26555. These observations are associated with program GO-14232. Some data presented in this paper were obtained from the Barbara A. Mikulski Archive for Space Telescopes (MAST). These data are associated with Programs GO-7402, GO-9049, and GO-14161. Other data have been obtained from the European Southern Observatory (ESO) Science Archive Facility. These data are associated with Programs 66.D-0636(A), 67.D-0439(A), 67.D-0554(A), 68.B-0475(A), 68.D-0094(A), 072.B-0585(A), and 095.D-0504(A). This research has also made use of the Keck Observatory Archive (KOA), which is operated by the W.M. Keck Observatory and the NASA Exoplanet Science Insti-

1. INTRODUCTION

The iron-group elements ( $21 \leq Z \leq 30$ ) observed in metal-poor stars were produced in massive-star supernovae early in the history of the Galaxy. Supernova models predict yields for individual elements as a function of initial mass, metallicity, rotation rate, and explosion physics. The predicted elemental abundance patterns can be incorporated into models of the chemical

tute (NExSci), under contract with NASA. This work has also made use of data collected from McDonald Observatory of the University of Texas at Austin.

evolution of the Galaxy or individual dwarf galaxies, where the yields, initial mass function, and supernova models are tuned and refined to reproduce the observed abundance patterns (e.g., [Nomoto et al. 2013](#)).

Yet concerns remain that the observed abundance patterns of the iron-group elements may not always be reliable. The singly-ionized species of iron-group elements dominate by number ( $\gtrsim 95\%$  for Sc through Cu; e.g., [Sneden et al. 2016](#)) in the line-forming layers of the atmospheres of late-type (FGK) stars. However, most of the lines detected in optical spectra accessible from the ground ( $3020 < \lambda \lesssim 10,000 \text{ \AA}$ ) arise from the neutral, minority species. This situation is further aggravated in the most metal-poor stars ( $[\text{Fe}/\text{H}] < -2.5$ ), because all metal lines get progressively weaker, and there are few if any lines of singly-ionized iron-group elements available in the optical. Lines from the neutral species may not always yield reliable abundances, because the assumption of local thermodynamic equilibrium (LTE) may be invalid when computing excitation and ionization equilibria in late-type, metal-poor stars (e.g., [Thévenin & Idiart 1999](#); [Korn et al. 2003](#); [Collet et al. 2005](#); [Mashonkina et al. 2011](#); [Bergemann et al. 2012](#); [Lind et al. 2012](#); [Ezzeddine et al. 2017](#)).

This issue can be avoided by deriving abundances from weak lines connected to the ground and low-lying levels of the majority, singly-ionized species. These levels contain the bulk of the populations, so they should not deviate appreciably from their LTE Boltzmann and Saha equilibria values. Lines of these species are plentiful in the near-ultraviolet (UV) portion of the spectrum ( $2000 \lesssim \lambda \lesssim 3100 \text{ \AA}$ ). This region of the spectrum is reasonably uncrowded in warm, metal-poor dwarf stars, so individual lines and the local continuum level can be discerned with confidence. Stars like these are ideal laboratories to test the reliability and applicability of LTE calculations to the analysis of iron-group abundances in metal-poor stars.

We adopted this approach in our pilot study of the warm, metal-poor dwarf HD 84937. [Sneden et al. \(2016\)](#) conducted an analysis of 446 Fe I lines and 105 Fe II lines in HD 84937, finding that the  $[\text{Fe}/\text{H}]$  ratios computed independently from the two species agreed to better than 0.01 dex, with a total systematic uncertainty less than 0.1 dex. [Sneden et al.](#) adopted model parameters for HD 84937 that were calculated independent of the spectra (see [Lawler et al. 2013](#)). This is an important point, because many abundance analyses of metal-poor stars lacking accurate parallax measurements rely on the ionization equilibrium of Fe I and II to determine the surface gravity. By construction, this approach forces both Fe I and Fe II lines to yield the same  $[\text{Fe}/\text{H}]$ , so it cannot be used to estimate possible non-LTE effects in Fe I. Furthermore, it may bias the derived surface gravity if Fe I is not in LTE (e.g., [Lind et al. 2012](#); [Sitnova et al. 2015](#)). [Sneden et al.](#) did not enforce ionization equilibrium, so their finding that both Fe I and II lines yield the

same  $[\text{Fe}/\text{H}]$  ratio is an independent confirmation that the deviations from LTE cannot be too severe. [Sneden et al.](#) also analyzed 152 Fe I and 16 Fe II lines in the Sun, where Fe I and Fe II lines each yielded  $[\text{Fe}/\text{H}]$  ratios that agreed at the 0.01 dex level.

As a natural extension of this study, we analyze six additional bright, metal-poor stars near the main-sequence turnoff point. Three of these stars with  $[\text{Fe}/\text{H}] \approx -2.9$ , BD+03°740, BD−13°3442, and CD−33°1173, form the core of the project for which new UV observations were obtained. Three other stars with high-quality archival UV spectra, G 64-12, HD 19445, and HD 94028, are included to provide benchmarks across a wider metallicity range ( $-3.3 \leq [\text{Fe}/\text{H}] \leq -1.6$ ) for abundances used in chemical evolution models. We also collect new and archival high-resolution optical spectra of all six stars. These observations are described in detail in [Section 2](#). We discuss our line list and transition probabilities in [Section 3](#), and we validate our data reduction by comparing equivalent widths (EWs) with previous work in [Section 4](#). We calculate stellar parameters using methods that are largely independent of the spectra in [Section 5](#). This enables us to independently assess the  $[\text{Fe}/\text{H}]$  values derived separately from Fe I and Fe II lines. We compare our derived Fe abundances with our previous work on HD 84937 in [Section 6](#). We discuss our results in [Section 7](#) and summarize our conclusions in [Section 8](#). Our complete analysis of other iron-group element abundances, and their implications for supernova yields and Galactic chemical evolution, will be presented in future work.

We adopt the standard definitions of elemental abundances and ratios. For element X, the logarithmic absolute abundance is defined as the number of atoms of X per  $10^{12}$  hydrogen atoms,  $\log \epsilon(X) \equiv \log_{10}(N_X/N_H) + 12.0$ . For elements X and Y, the logarithmic abundance ratio relative to the Solar ratio is defined as  $[X/Y] \equiv \log_{10}(N_X/N_Y) - \log_{10}(N_X/N_Y)_\odot$ . We adopt the Solar Fe abundance of [Asplund et al. \(2009\)](#),  $\log \epsilon(\text{Fe}) = 7.50$ . Abundances or ratios denoted with the ionization state are defined to be the total elemental abundance as derived from transitions of that particular ionization state after Saha ionization corrections have been applied.

## 2. OBSERVATIONS

Our analysis is based on several new sets of UV spectra, supplemented with new or archival UV and optical spectra. These spectra cover most of the near-UV and optical spectral ranges of each of the six stars. [Table 1](#) lists some key features of the spectra, including the instrument, program identification (ID) number, principle investigator (PI), wavelength range covered ( $\lambda$ ), spectral resolving power ( $R \equiv \lambda/\Delta\lambda$ ), and signal-to-noise (S/N) ratio at a representative wavelength.

The new UV spectra were obtained using the Space Telescope Imaging Spectrograph (STIS; [Kimble et al.](#)

**Table 1.** Characteristics of Near-UV and Optical Spectra

| Star                          | Instrument | Program ID            | PI                     | $\lambda$ (Å) | $R$     | S/N pix <sup>-1</sup> @ $\lambda$ |
|-------------------------------|------------|-----------------------|------------------------|---------------|---------|-----------------------------------|
| BD+03°740<br>( $V = 9.81$ )   | STIS       | GO-14232 <sup>a</sup> | Roederer               | 2278–3068     | 30,000  | 70@2820 Å                         |
|                               | UVES       | 68.D-0094(A)          | Primas                 | 3050–3869     | 41,000  | 230@3500 Å                        |
|                               | HIRES      | H41aH                 | Boesgaard <sup>i</sup> | 3568–3950     | 47,000  | 280@3650 Å                        |
|                               | Tull       | ...                   | Sneden                 | 3680–10120    | 33,000  | 180@5100 Å                        |
|                               | HIRES      | U10H                  | Bolte <sup>j</sup>     | 3970–4917     | 47,000  | 200@4500 Å                        |
|                               | UVES       | 68.D-0094(A)          | Primas                 | 4780–5755     | 51,000  | 480@5100 Å                        |
|                               | UVES       | 68.D-0094(A)          | Primas                 | 5834–6804     | 51,000  | 320@6000 Å                        |
| BD–13°3442<br>( $V = 10.27$ ) | STIS       | GO-14232 <sup>b</sup> | Roederer               | 2278–3069     | 30,000  | 60@2820 Å                         |
|                               | UVES       | 67.D-0439(A)          | Primas <sup>k</sup>    | 3060–3867     | 49,000  | 125@3500 Å                        |
|                               | UVES       | 095.D-0504(A)         | Melendez <sup>l</sup>  | 3300–4515     | 49,000  | 110@4000 Å                        |
|                               | UVES       | 67.D-0439(A)          | Primas <sup>k</sup>    | 4785–5755     | 57,000  | 230@5100 Å                        |
|                               | UVES       | 67.D-0439(A)          | Primas <sup>k</sup>    | 5833–6805     | 57,000  | 210@6000 Å                        |
| CD–33°1173<br>( $V = 10.90$ ) | STIS       | GO-14232 <sup>c</sup> | Roederer               | 2277–3069     | 30,000  | 55@2820 Å                         |
|                               | UVES       | 68.B-0475(A)          | Primas                 | 3050–3867     | 37,000  | 160@3500 Å                        |
|                               | UVES       | 095.D-0504(A)         | Melendez               | 3305–4520     | 49,000  | 90@4000 Å                         |
|                               | UVES       | 68.B-0475(A)          | Primas                 | 4887–5755     | 46,000  | 200@5100 Å                        |
|                               | UVES       | 68.B-0475(A)          | Primas                 | 5832–6806     | 46,000  | 190@6000 Å                        |
| G 64-12<br>( $V = 11.45$ )    | STIS       | GO-9049 <sup>d</sup>  | Deliyannis             | 2001–2812     | 30,000  | 25@2820 Å                         |
|                               | HIRES      | H11aH                 | Boesgaard <sup>i</sup> | 3070–3903     | 49,000  | 250@3500 Å                        |
|                               | UVES       | 67.D-0554(A)          | Christlieb             | 3297–4490     | 41,000  | 150@4000 Å                        |
|                               | UVES       | 67.D-0554(A)          | Christlieb             | 4810–5727     | 42,000  | 250@5100 Å                        |
|                               | UVES       | 67.D-0554(A)          | Christlieb             | 5824–6795     | 42,000  | 240@6000 Å                        |
| HD 19445<br>( $V = 8.06$ )    | STIS       | GO-7402 <sup>e</sup>  | Peterson <sup>m</sup>  | 2313–3067     | 30,000  | 65@2820 Å                         |
|                               | UVES       | 68.D-0094(A)          | Primas <sup>k</sup>    | 3055–3874     | 41,000  | 200@3500 Å                        |
|                               | UVES       | 66.D-0636(A)          | Piotto <sup>n</sup>    | 3760–4980     | 41,000  | 220@4500 Å                        |
|                               | UVES       | 68.D-0094(A)          | Primas <sup>k</sup>    | 4790–5760     | 51,000  | 300@5100 Å                        |
|                               | UVES       | 68.D-0094(A)          | Primas <sup>k</sup>    | 5841–6810     | 51,000  | 200@6000 Å                        |
| HD 84937<br>( $V = 8.32$ )    | STIS       | GO-7402 <sup>f</sup>  | Peterson <sup>m</sup>  | 2279–3117     | 30,000  | 55@2820 Å                         |
|                               | STIS       | GO-14161 <sup>g</sup> | Peterson <sup>o</sup>  | 2128–3143     | 114,000 | 50@2820 Å                         |
| HD 94028<br>( $V = 8.22$ )    | STIS       | GO-7402 <sup>f</sup>  | Peterson <sup>m</sup>  | 2280–3117     | 30,000  | 40@2820 Å                         |
|                               | STIS       | GO-14161 <sup>h</sup> | Peterson <sup>o</sup>  | 2128–3143     | 114,000 | 40@2820 Å                         |
|                               | UVES       | 072.B-0585(A)         | Silva                  | 3050–3860     | 37,000  | 70@3500 Å                         |
|                               | Tull       | ...                   | Roederer <sup>p</sup>  | 3650–8000     | 33,000  | 140@5100 Å                        |

<sup>a</sup> Datasets OCTS01010, OCTS02010-30

<sup>b</sup> Datasets OCTS03010-30, OCTS04010-20, OCTS05010-20

<sup>c</sup> Datasets OCTS06010-30, OCTS07010-30, OCTS08010-30

<sup>d</sup> Datasets O6ED01010-20, O6ED02010-20, O6ED03010-20, O6ED04010-20

<sup>e</sup> Datasets 056D01010, 056D03010

<sup>f</sup> Dataset 056D06010

<sup>g</sup> Datasets OCTKA6010-D020

<sup>h</sup> Datasets OCTKB0010-6030

<sup>i</sup> See [Rich & Boesgaard \(2009\)](#)

<sup>j</sup> See [Lai et al. \(2008\)](#)

<sup>k</sup> See [Hansen et al. \(2012\)](#)

<sup>l</sup> See [Reggiani et al. \(2017\)](#)

<sup>m</sup> See [Peterson et al. \(2001\)](#)

<sup>n</sup> See [Recio-Blanco et al. \(2002\)](#)

<sup>o</sup> See [Peterson et al. \(2017\)](#)

<sup>p</sup> See [Roederer et al. \(2014\)](#)

1998; Woodgate et al. 1998) on the *Hubble Space Telescope* (*HST*). These observations were made using the E230M echelle grating centered at  $\lambda 2707$ , the  $0''.06 \times 0''.2$  slit, the near-UV Multianode Microchannel Array (MAMA) detector. Three stars were observed with STIS as part of Program GO-14232: BD+03°740, BD−13°3442, and CD−33°1173. BD+03°740 was observed over the course of four orbits, or 9,556 s of integration time, on 2016 Feb 16 and 2016 Mar 27. BD−13°3442 was observed over the course of seven orbits, or 17,264 s of integration time, on 2016 Dec 22 and 2016 Dec 24. CD−33°1173 was observed over the course of nine orbits, or 23,355 s of integration time, on 2016 Dec 31, 2017 Jan 01, and 2017 Jan 06-08. The total counts in these observations generally increase by factors of 2–3 from the shortest wavelengths to  $\sim 2800$  Å, where the reference S/N is listed in Table 1. Figure 1 illustrates a portion of the UV spectrum of these stars.

Additional spectra are obtained from a variety of online archives, including the Mikulski Archive for Space Telescopes (MAST), the European Southern Observatory (ESO) Science Archive Facility, and the Keck Observatory Archives. These include data collected using the Ultraviolet and Visual Echelle Spectrograph (UVES; Dekker et al. 2000) at the Very Large Telescope (VLT UT2) and the High Resolution Echelle Spectrometer (HIRES; Vogt et al. 1994) at the Keck I Telescope. The footnotes of Table 1 reference publications by the original investigators that describe these data in detail.

We also make use of spectra obtained using the Robert G. Tull Coudé Spectrograph (Tull et al. 1995) at the Harlan J. Smith Telescope at McDonald Observatory. The Tull spectrum of HD 94028 has been described previously by Roederer et al. (2014). The Tull spectrum

of BD+03°740 was obtained on 2016 Oct 21, with an integration time of 2100 s, using an identical setup and following similar calibration and reduction procedures.

### 3. LINE LIST AND TRANSITION PROBABILITIES

We prioritize  $\log gf$  values derived from modern laboratory studies that use radiative lifetime measurements from laser-induced fluorescence and emission branching fraction data from high resolution spectrometers. This approach routinely achieves high precision absolute  $\log gf$  values whose uncertainties are  $\approx 5\%$  or better. We adopt an initial Fe I line list from Sneden et al. (2016), who made use of laboratory  $\log gf$  values published by O’Brian et al. (1991), via the National Institute of Standards and Technology (NIST) Atomic Spectral Database (ASD) (Kramida et al. 2017), and recent work by Den Hartog et al. (2014) and Ruffoni et al. (2014). The median uncertainty in the  $\log gf$  values for the lines measured in at least one star in our sample is  $\approx 7\%$  (NIST grade B+), or  $\approx 0.03$  dex.

Our initial Fe II line list also comes from Sneden et al. (2016), who adopted the  $\log gf$  values from NIST. Modern laboratory work on Fe II lines is not as extensive as for Fe I, and the median uncertainty of the lines in our list is  $\approx 25\%$  (NIST grade C), or  $\approx 0.12$  dex. The NIST values are adopted from many studies, including Bergeson et al. (1996), Sikström et al. (1999), Pickering et al. (2001, 2002), and Schnabel et al. (2004). Comparisons by Bergeson et al. between their results and values in the NIST ASD at that time indicated that no serious systematic differences were present. The list of Fe I and II lines measured in at least one star in our sample is given in Table 2.

**Table 2.** Fe Line List, Equivalent Widths, and Abundances

| Species | Wavelength | E.P. | $\log gf$ | EW   | $\log \epsilon$ |
|---------|------------|------|-----------|------|------|------|------|------|------|------|-----------------|-----------------|-----------------|-----------------|-----------------|-----------------|-----------------|
|         | (Å)        | (eV) |           | (mÅ) | [1]             | [2]             | [3]             | [4]             | [5]             | [6]             | [7]             |
|         |            |      |           | [1]  | [2]  | [3]  | [4]  | [5]  | [6]  | [7]  | [1]             | [2]             | [3]             | [4]             | [5]             | [6]             | [7]             |
| Fe I    | 2297.79    | 0.05 | −1.10     | ...  | ...  | 53.3 | ...  | ...  | ...  | ...  | ...             | ...             | 4.817           | ...             | ...             | ...             | ...             |
| Fe I    | 2369.46    | 0.11 | −2.19     | 20.6 | 22.7 | ...  | ...  | ...  | ...  | ...  | 4.616           | 4.741           | ...             | ...             | ...             | ...             | ...             |
| Fe I    | 2371.43    | 0.09 | −1.95     | 34.8 | 42.5 | 28.2 | 23.7 | 64.0 | ...  | 75.5 | 4.749           | 5.055           | 4.843           | 4.591           | 5.589           | ...             | 6.069           |

NOTE—[1] BD+03°740; [2] BD−13°3442; [3] CD−33°1173; [4] G 64-12; [5] HD 19445; [6] HD 84937; [7] HD 94028

NOTE—The complete version of Table 2 is available in the online edition of the journal. An abbreviated version is shown here to illustrate its form and content.

Previous studies (e.g., Cayrel et al. 2004; Cohen et al. 2008, 2013; Lai et al. 2008) have found that Fe I lines with low excitation potentials (E.P.) may yield LTE abundances higher than average in metal-poor dwarfs and giants. Bergemann et al. (2012) confirmed this phenomenon in their models and advocated using Fe II and

high-excitation Fe I lines in determining metallicities. We have many low-E.P. Fe I lines in our list, and we measure EWs for and derive abundances from these lines. We report these values in Table 2, but we exclude Fe I lines with E.P.  $< 1.2$  eV from our adopted abundance calculations, following recommendations from the studies referenced previously. As we discuss in Section 7.1,

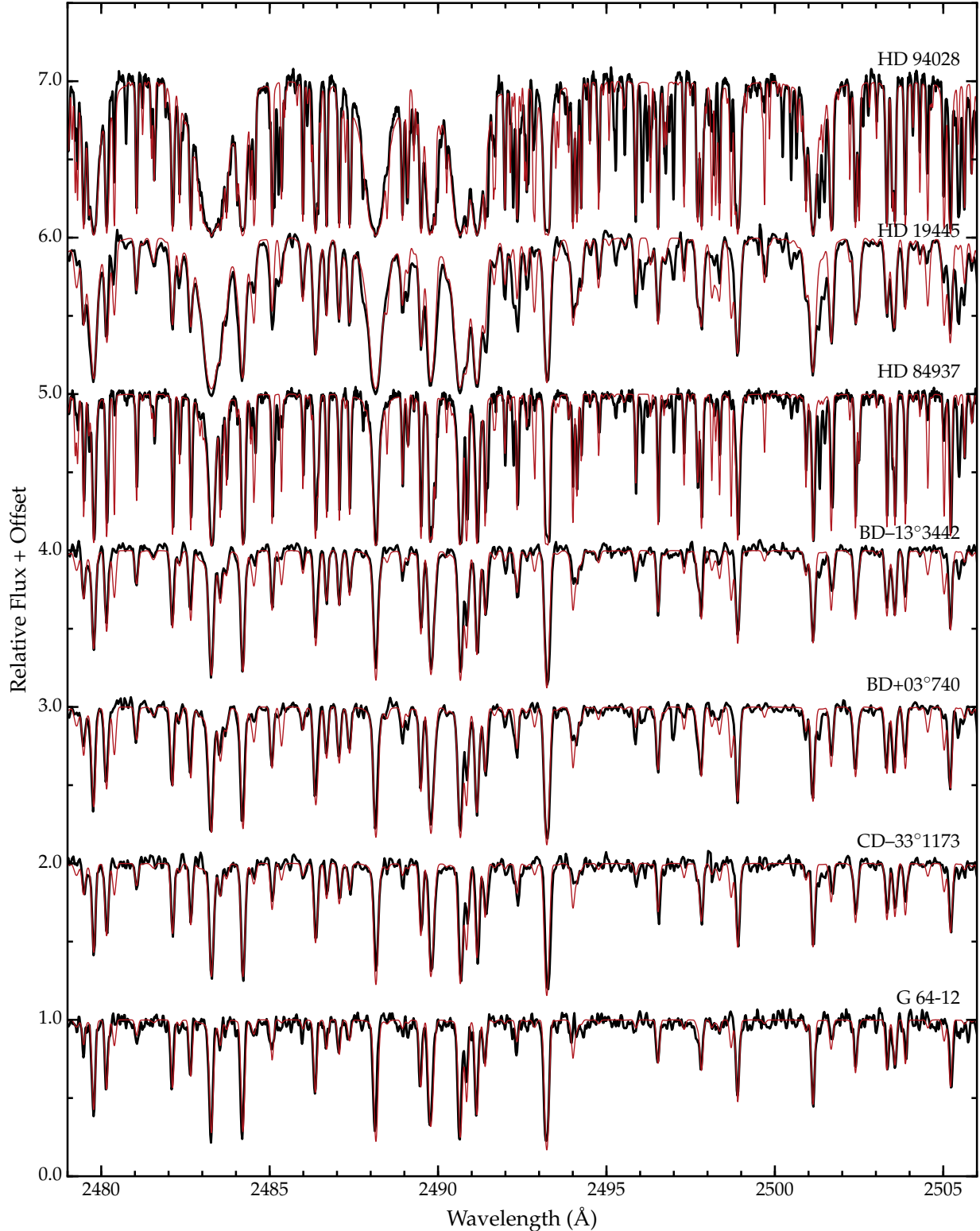


**Figure 1.** Portions of the STIS UV spectra of the six stars in our sample, plus HD 84937. The spectra are normalized to unity and offset vertically to enhance visibility. The bold black lines mark the observed spectra, and the thin red lines mark the synthetic spectra. The overwhelming majority of lines in this region are due to neutral and singly-ionized species of Fe group elements (Sc through Ni). We adopt abundance ratios  $[X/Fe]$  for these iron-group elements, X, from previous work (Aoki et al. 2006; Lai et al. 2008; Roederer et al. 2014; Sneden et al. 2016; Reggiani et al. 2017) and averaged together these ratios in cases with no previous values. Note that the spectra of HD 84937 and HD 94028 were taken with STIS/E230H ( $R \sim 114,000$ ), and the other spectra were taken with STIS/E230M ( $R \sim 30,000$ ); see Section 4.3 for details.

the Fe I lines with E.P.  $< 1.2$  eV do yield higher abundances than the lines with E.P.  $> 1.2$  eV in our study, although the magnitude of the difference in the mean is small ( $\leq 0.03$  dex) in six of the seven stars.

#### 4. EQUIVALENT WIDTHS

We measure EWs using a semi-automatic routine that fits Voigt or Gaussian line profiles to continuum-normalized spectra at wavelengths of interest (see [Roederer et al. 2014](#)). Upon visual inspection of each line in each star, any line determined to be undetected, blended, suffer from uncertain continuum placement, or otherwise compromised is discarded from consideration. The EWs are listed in [Table 2](#).

##### 4.1. Comparisons with Other Optical Spectra

We deliberately obtain several sets of spectra of BD+03°740 that overlap in wavelength to check the reproducibility of the EW measurements. For a set of 49 lines in common between the UVES and Tull spectra of BD+03°740, we find a difference (UVES–Tull) of  $-0.5 \pm 0.3$  mÅ ( $\sigma = 1.8$  mÅ). For a set of 28 lines in common between the HIRES and Tull spectra of BD+03°740, we find a difference (HIRES–Tull) of  $+0.3 \pm 0.6$  mÅ ( $\sigma = 3.3$  mÅ). These differences are small and not significant. We regard the spectra as interchangeable, although we prioritize the one with higher S/N and resolving power in regions of overlap.

##### 4.2. Comparisons with Previous Work

We also use BD+03°740 to compare our EW measurements to those made by other investigators. Studies with at least 5 published EWs in common with us are listed in [Table 3](#). The mean differences and standard deviations are small, indicating that our EWs are in good agreement with previous studies of this star. These internal and external comparisons support our assertion that our method of measuring EWs is reliable within the range of stellar parameters and quality of the spectra used in the present study.

##### 4.3. Comparisons with Higher Resolution UV Spectra

Higher-resolution archival STIS spectra covering the same UV wavelength region are available for HD 84937 and HD 94028, as pointed out by the referee. These spectra were taken using the E230H grating, which provides a resolving power  $R \sim 114,000$ . We download, co-add, and continuum normalize these spectra using the same approach used for the E230M  $R \sim 30,000$  spectra. [Table 1](#) lists the characteristics of these spectra.

To determine what impact the spectral resolution may have on our EW measurements, we compare the EWs of UV lines measured in the E230M spectra of HD 84937 and HD 94028 to those measured in the E230H spectra. These values are listed in [Table 4](#). For HD 84937, the mean difference in the EW measurements (E230M minus E230H) is  $+0.5 \pm 0.5$  mÅ ( $\sigma = 4.7$  mÅ, 93 lines).

**Table 3.** Comparison of Equivalent Width Measurements of BD+03°740 with Previous Studies

| Previous study                              | Mean difference <sup>a</sup> | Standard deviation | Number of lines |
|---|------------------------------|--------------------|-----------------|
|   | (mÅ)                         | (mÅ)               |                 |
| <a href="#">Fulbright (2000)</a>            | $0.0 \pm 0.7$                | 2.1                | 8               |
| <a href="#">Carretta et al. (2002)</a>      | $+1.0 \pm 0.3$               | 1.2                | 24              |
| <a href="#">Ivans et al. (2003)</a>         | $+2.1 \pm 0.7$               | 3.8                | 27              |
| <a href="#">Lai et al. (2008)</a>           | $-0.7 \pm 0.3$               | 2.1                | 64              |
| <a href="#">Hosford et al. (2009)</a>       | $+2.0 \pm 0.6$               | 4.3                | 51              |
| <a href="#">Rich &amp; Boesgaard (2009)</a> | $+1.2 \pm 0.6$               | 2.6                | 19              |

<sup>a</sup> In the sense of  $EW_{\text{previous}} - EW_{\text{this study}}$

For HD 94028, the mean difference is  $-0.9 \pm 2.3$  mÅ ( $\sigma = 6.6$  mÅ, 8 lines). Neither difference is significant.

**Table 4.** Comparison of Fe Equivalent Widths and Abundances from E230M and E230H Spectra

| Star    | Species | $\lambda$ | E.P. | $\log gf$ | EW   | EW   | $\log \epsilon$ | $\log \epsilon$ | $\log \epsilon$ | $\log \epsilon$ |
|---------|---------|-----------|------|-----------|------|------|-----------------|-----------------|-----------------|-----------------|
|         |         | (Å)       | (eV) |           | (mÅ) | (mÅ) | [3]             | [4]             | [5]             | [6]             |
|         |         |           |      |           | [1]  | [2]  |                 |                 |                 |                 |
| HD84937 | FeI     | 2297.79   | 0.05 | -1.10     | 66.1 | 67.0 | 5.225           | 5.256           | 5.27            | 5.32            |
| HD84937 | FeI     | 2299.22   | 0.09 | -1.55     | 54.4 | 60.3 | 5.227           | 5.472           | 5.27            | 5.26            |
| HD84937 | FeI     | 2369.46   | 0.11 | -2.19     | 33.1 | 38.1 | 5.073           | 5.222           | 5.12            | 5.24            |

*Table 4 continued*

**Table 4** (*continued*)

| Star | Species | $\lambda$ | E.P. | $\log gf$ | EW   | EW   | $\log \epsilon$ | $\log \epsilon$ | $\log \epsilon$ | $\log \epsilon$ |
|------|---------|-----------|------|-----------|------|------|-----------------|-----------------|-----------------|-----------------|
|      |         | (Å)       | (eV) |           | (mÅ) | (mÅ) | [1]             | [2]             | [3]             | [4]             |
|      |         |           |      |           |      |      | [1]             | [2]             | [3]             | [4]             |

NOTE—[1] EW measured in E230M spectrum; [2] EW measured in E230H spectrum; [3]  $\log \epsilon$  abundance derived from EW measured in E230M spectrum; [4]  $\log \epsilon$  abundance derived from EW measured in E230H spectrum; [5]  $\log \epsilon$  abundance derived from synthesis of E230M spectrum (Snedén et al. 2016 in the case of HD 84937, this study in the case of HD 94028); [6]  $\log \epsilon$  abundance derived from synthesis of E230H spectrum

NOTE—The complete version of Table 2 is available in the online edition of the journal. An abbreviated version is shown here to illustrate its form and content.

## 5. STELLAR PARAMETERS

We calculate the effective temperature ( $T_{\text{eff}}$ ) and  $\log$  of the surface gravity ( $\log g$ ) of each star using methods that are largely independent of our spectra. We use metallicity-dependent calibrations to calculate  $T_{\text{eff}}$  from broadband colors, but these calibrations have only a weak dependence on metallicity for metal-poor stars. The  $\log g$  value is calculated from two parameters with mild metallicity dependencies, bolometric correction and  $T_{\text{eff}}$ . The microturbulent velocity ( $v_t$ ) and metallicity of the model atmosphere ( $[M/H]$ ) are determined iteratively along with the Fe abundance, so these parameters depend on the spectra. The effects of  $[M/H]$  on  $v_t$  are expected to be small ( $< 0.1 \text{ km s}^{-1}$ ), however, over the parameter range of interest (Lind et al. 2012).

### 5.1. Effective Temperatures

We compile optical and near infrared broadband photometry using catalogs from Ducati (2002) and Munari et al. (2014) for Johnson  $B$  and  $V$ ; Cutri et al. (2003) for 2MASS  $J$ ,  $H$ , and  $K$ ; and Paunzen (2015) for Strömberg-Crawford  $b$  and  $y$ . We construct six colors ( $B - V$ ,  $V - J$ ,  $V - H$ ,  $V - K$ ,  $J - K$ , and  $b - y$ ) from these data.

We adopt reddening estimates from Casagrande et al. (2011), when available, otherwise we modify the reddening predicted by the Schlafly & Finkbeiner (2011) dust maps. These stars are nearby and in the foreground of some of the reddening layer, so we reduce the Schlafly & Finkbeiner reddening estimates by multiplying  $E(B - V)$  by  $1 - \exp(-|d \sin b|/h)$  (Bonifacio et al. 2000). Here,  $d$  is the distance to the star (Section 5.2), and  $b$  is its Galactic latitude. Following Bonifacio et al., we assume a scale height,  $h$ , of 125 pc for the reddening layer. The  $E(B - V)$  values from the Casagrande et al. catalog and the reduced Schlafly & Finkbeiner values are always small,  $< 0.025$ .

We independently estimate the reddening using interstellar Na I absorption visible in the spectra. The ratios of the EWs of the interstellar doublet lines at 5889.95 and 5895.92 Å are  $\approx 2$ , which matches the ratio of their  $f$ -values. This indicates an optically thin col-

**Table 5.** Reddening Estimates

| Star        | $E(B - V)$ | $E(B - V)$ | $E(B - V)$ | $E(B - V)$ |
|-------------|------------|------------|------------|------------|
|             | [1]        | [2]        | [3]        | [4]        |
| BD+03° 740  | 0.00       | 0.020      | 0.022      | 0.018      |
| BD−13° 3442 | ...        | 0.025      | 0.011      | 0.012      |
| CD−33° 1173 | ...        | 0.010      | 0.005      | 0.003      |
| G 64-12     | ...        | 0.021      | 0.003      | 0.008      |
| HD 19445    | 0.00       | 0.019      | 0.000      | $< 0.002$  |
| HD 84937    | 0.00       | 0.012      | 0.005      | 0.007      |
| HD 94028    | 0.00       | 0.007      | 0.000      | $< 0.001$  |

NOTE—[1] Casagrande et al. (2011) color calibrations; [2] Schlafly & Finkbeiner (2011) dust maps, reduced as described in Section 5.1; [3] Na I, Meléndez et al. (2010); [4] Na I, this study.

umn. Following Alves-Brito et al. (2010) and Roederer et al. (2012), we transform the EW into the Na I column density as given by Spitzer (1968), the Na I column density into the H column density as given by Ferlet et al. (1985), and the H column density into  $E(B - V)$  as given by Bohlin et al. (1978). The typical statistical uncertainties using this method are  $\approx 0.002$  mag, ignoring uncertainties in the calibrations themselves.  $E(B - V) \leq 0.018$  in all cases, in agreement with other estimates, as reported in Table 5. We deredden according to the extinction coefficients of McCall (2004).

We adopt the  $T_{\text{eff}}$  values calculated according to the metallicity-dependent color- $T_{\text{eff}}$  calibrations given by Casagrande et al. (2010). We estimate  $T_{\text{eff}}$  from each color by drawing  $10^4$  samples from each input parameter (magnitudes, reddening, and metallicity), assuming Gaussian uncertainties. We adopt a minimum uncertainty of 0.02 mag in magnitude, 0.02 mag in  $E(B - V)$ , and 0.3 dex in metallicity. Not all  $T_{\text{eff}}$  values for a given star are independent, because some magnitudes are used to construct multiple colors. The same set of input draws is employed within each of the  $10^4$  trials, however, so each calculation is self-consistent. Table 6 lists the median  $T_{\text{eff}}$  values predicted by each color for each star. The uncertainty in  $T_{\text{eff}}$  from a given color is calculated as the quadrature sum of the standard deviation of the  $10^4$  values of  $T_{\text{eff}}$  and the uncertainty in the

calibration itself. The final  $T_{\text{eff}}$  value is calculated as the average of the individual color predictions, weighted by their inverse-square uncertainties. These values and their statistical uncertainties (stat.) are listed in the final column of Table 6.

We estimate the systematic uncertainty (sys.) in  $T_{\text{eff}}$  using the standard deviation of the average  $T_{\text{eff}}$  values predicted by this color- $T_{\text{eff}}$  scale and those of [Alonso et al. \(1999\)](#) and [Ramírez & Meléndez \(2005\)](#). These other scales provide calibrations for only four ([Alonso et al.](#)) and five ([Ramírez & Meléndez](#)) of the colors available to us. The total uncertainties, which represent the quadrature sum of the statistical and systematic uncertainties, are reported in Table 7.

### 5.2. Surface Gravity

We calculate  $\log g$  from fundamental relations:

$$\log g = 4 \log T_{\text{eff}} + \log(M/M_{\odot}) - 10.61 + 0.4(BC_V + m_V - 5 \log d + 5 - 3.1E(B - V) - M_{\text{bol},\odot}). \quad (1)$$

Here,  $M$  is the mass of the star, which is always assumed to be  $0.8 \pm 0.2 M_{\odot}$ .  $BC_V$  is the bolometric correction in the  $V$  band ([Casagrande & Vandenberg 2014](#)).  $m_V$  is the apparent  $V$  magnitude.  $d$  is the distance in pc, which is calculated from parallaxes reported in the first *Gaia* data release (DR1; [Gaia Collaboration et al. 2016](#)). These values make use of the combined *Tycho-2* and *Gaia* catalogs. *Gaia* DR1 did not report a parallax for HD 84937 (Section 6.1), so we use the parallax measured by *Hipparcos* using the data reduction by [van Leeuwen \(2007\)](#). This value,  $13.74 \pm 0.78$  mas, is slightly larger than the one measured using the Fine Guidance Sensors on *HST* by [Vandenberg et al. \(2014\)](#),  $12.24 \pm 0.20$  mas. The  $\log g$  value calculated by [Vandenberg et al.](#), 4.05, falls within the uncertainties of the one calculated from the *Hipparcos* parallax,  $4.16 \pm 0.14$ . For the other stars in our sample, the *Gaia* and *Hipparcos* parallaxes agree to within  $\approx 1.5$  times their stated uncertainties, and the *Gaia* uncertainties are typically smaller by  $\approx 70$ – $90\%$ .  $M_{\text{bol},\odot}$  is the solar bolometric magnitude, 4.75. The constant 10.61 is calculated from the solar constants  $\log T_{\text{eff},\odot} = 3.7617$  and  $\log g_{\odot} = 4.438$ . We draw  $10^4$  samples from each of these input parameters to estimate the uncertainty in  $\log g$ . The  $\log g$  value for each star reported in Table 7 represents the median of these realizations, and the uncertainty in  $\log g$  reported in Table 7 is their standard deviation.

We also compare the abundances derived from the pressure-sensitive wings of Mg I and II lines as an independent check of the  $\log g$  values. The abundances derived from syntheses of the two species should agree if the  $\log g$  value is approximately correct. The Mg I line at 5183.60 Å has broad wings in only two stars in our sample, HD 19445 and HD 94028. STIS spectra cover the Mg I resonance line at 2852.13 Å (except in G 64-12) and the Mg II resonance doublet at 2795.53

and 2802.71 Å. The  $\log gf$  values for all four of these lines are known to better than 3% ([Kramida et al. 2017](#)), and [Barklem et al. \(2000\)](#) calculated damping constants for these lines. The abundance uncertainties are typically 0.05–0.10 dex and are dominated by uncertainties in the continuum placement around the broad ( $\approx 15$ – $30$  Å) Mg II lines. The Mg abundances derived from profile fits agree in all cases, which supports our adopted  $\log g$  values.

Figure 2 compares the  $T_{\text{eff}}$  and  $\log g$  for the six stars in our sample with a set of isochrones for old (10 and 13 Gyr), metal-poor ( $[\text{Fe}/\text{H}] = -1.5$  and  $-2.5$ ),  $\alpha$ -enhanced ( $[\alpha/\text{Fe}] = +0.4$ ) stellar populations with standard He mass fractions (0.2452 and 0.2468) downloaded from the Dartmouth Stellar Evolution Database ([Dotter et al. 2008](#)). Several of these stars appear to lie along isochrones that are  $\sim 1$  dex more metal rich or those that would be several Gyr older than the age of the Universe. Both scenarios are clearly unrealistic. The same effect occurs if the PARSEC isochrones ([Bressan et al. 2012](#); [Marigo et al. 2017](#)) are used instead. Resolving this matter is beyond the scope of the present study, and we underscore that the main conclusion we draw from Figure 2 is that the stars in our sample are found on the main sequence or just slightly evolved beyond it.

### 5.3. Microturbulent Velocity, Metallicity, and Fe Abundances

We interpolate model atmospheres from the  $\alpha$ -enhanced ATLAS9 grid of models ([Castelli & Kurucz 2003](#)), using an interpolation code provided by A. McWilliam (2009, private communication). We derive abundances using a recent version of the line analysis software MOOG ([Snedden 1973](#); [Sobeck et al. 2011](#); 2017 version). These calculations assume that LTE holds in the line-forming layers of the atmosphere. This version of MOOG can calculate the contribution of Rayleigh scattering to the continuous opacity either as pure absorption or as isotropic, coherent scattering, and we investigate the impact of these methods in Section 5.6.4. We use the damping constants from [Barklem et al. \(2000\)](#) and [Barklem & Aspelund-Johansson \(2005\)](#), when available. Otherwise, we resort to the standard [Unsöld \(1955\)](#) recipe. We exclude strong lines with  $\log(\text{EW}/\lambda) > -4.4$  from consideration.

We begin by adopting a microturbulent velocity of  $1.5 \text{ km s}^{-1}$  and model metallicity consistent with previous analyses of each star. We iteratively determine  $v_t$ ,  $[\text{M}/\text{H}]$ , and the Fe abundances derived from Fe I and II lines. During these iterations, we cull lines whose abundance deviates by more than 0.4 dex from the mean for each species. We set  $v_t$  when there is no dependence of abundance derived from Fe I lines on line strength. We set  $[\text{M}/\text{H}]$  to be the average Fe abundance derived from Fe I and II lines, rounded to the nearest 0.05 dex. Small changes in  $[\text{M}/\text{H}]$  have minimal impact on the derived abundances. The  $v_t$  and  $[\text{M}/\text{H}]$  values are listed

**Table 6.** Temperatures Predicted by Casagrande et al. Color Calibrations

| Star       | $T_{\text{eff}}$<br>( $B - V$ )<br>(K) | $T_{\text{eff}}$<br>( $V - J$ )<br>(K) | $T_{\text{eff}}$<br>( $V - H$ )<br>(K) | $T_{\text{eff}}$<br>( $V - K$ )<br>(K) | $T_{\text{eff}}$<br>( $J - K$ )<br>(K) | $T_{\text{eff}}$<br>( $b - y$ )<br>(K) | $T_{\text{eff}}$<br>(adopted)<br>(K) |
|------------|--|--|--|--|--|--|--------------------------------------|
| BD+03°740  | 6589 ± 175                             | 6257 ± 90                              | 6272 ± 92                              | 6324 ± 77                              | 6570 ± 278                             | 6475 ± 89                              | 6351 ± 51                            |
| BD−13°3442 | 6447 ± 168                             | 6346 ± 102                             | 6353 ± 80                              | 6402 ± 64                              | 6611 ± 262                             | 6530 ± 110                             | 6405 ± 49                            |
| CD−33°1173 | 6522 ± 167                             | 6609 ± 111                             | 6665 ± 94                              | 6629 ± 82                              | 6642 ± 257                             | 6619 ± 100                             | 6625 ± 53                            |
| G 64-12    | 6516 ± 185                             | 6475 ± 105                             | 6507 ± 82                              | 6447 ± 69                              | 6481 ± 259                             | 6575 ± 105                             | 6492 ± 51                            |
| HD 19445   | 6093 ± 147                             | 5987 ± 80                              | 6071 ± 83                              | 6062 ± 57                              | 6281 ± 217                             | 6044 ± 196                             | 6055 ± 46                            |
| HD 84937   | 6562 ± 168                             | 6386 ± 91                              | 6424 ± 75                              | 6382 ± 62                              | 6370 ± 215                             | 6495 ± 94                              | 6418 ± 44                            |
| HD 94028   | 6088 ± 145                             | 6030 ± 80                              | 6047 ± 67                              | 6105 ± 55                              | 6299 ± 207                             | 6130 ± 82                              | 6087 ± 40                            |

**Table 7.** Stellar Parameters

| Star                  | $T_{\text{eff}}$<br>(K) | $\log g$    | $v_t$<br>(km s <sup>−1</sup> ) | [M/H]       |
|-----------------------|-------------------------|-------------|--------------------------------|-------------|
| BD+03°740             | 6351 ± 73               | 3.97 ± 0.13 | 1.70 ± 0.2                     | −2.90 ± 0.1 |
| BD−13°3442            | 6405 ± 74               | 4.04 ± 0.15 | 1.60 ± 0.2                     | −2.85 ± 0.1 |
| CD−33°1173            | 6625 ± 137              | 4.29 ± 0.14 | 1.60 ± 0.2                     | −3.00 ± 0.1 |
| G 64-12               | 6492 ± 103              | 4.18 ± 0.21 | 1.55 ± 0.2                     | −3.30 ± 0.1 |
| HD 19445              | 6055 ± 78               | 4.49 ± 0.13 | 1.20 ± 0.2                     | −2.20 ± 0.1 |
| HD 84937 <sup>a</sup> | 6418 ± 117              | 4.16 ± 0.14 | 1.50 ± 0.2                     | −2.25 ± 0.1 |
| HD 94028              | 6087 ± 84               | 4.37 ± 0.13 | 1.10 ± 0.2                     | −1.60 ± 0.1 |

<sup>a</sup> Rederived; see Section 6.1

in Table 7, and the derived Fe abundances and number of lines used are listed in Table 8.

We estimate systematic uncertainties on the metallicities derived from Fe I lines, Fe II lines, and their difference by drawing 10<sup>3</sup> samples from each input parameter in the model atmosphere ( $T_{\text{eff}}$ ,  $\log g$ ,  $v_t$ , and [M/H]) from normal distributions using the mean values and their uncertainties listed in Table 7. A new model atmosphere is interpolated for each of these 10<sup>3</sup> draws, and the abundances are recomputed for each line. We also include an EW uncertainty of 5% for each line in these calculations. We adopt the median of these 10<sup>3</sup> realizations as the average Fe abundance and the standard deviation as the systematic uncertainty.

#### 5.4. Comparison between Abundances Derived from Spectra with Different Resolving Powers

We showed in Section 4.3 that the EWs measured from STIS E230M  $R \sim 30,000$  and E230H  $R \sim 114,000$  are statistically identical for HD 84937 and HD 94028. We now compare the abundances derived from these two sets of EW values. The two sets of EWs yield a difference (in the sense of E230M minus E230H) of  $+0.014 \pm 0.016$  ( $\sigma = 0.15$ , 93 lines) in HD 84937 and  $-0.019 \pm 0.060$  ( $\sigma = 0.17$ , 8 lines) in HD 94028. Unsurprisingly, neither difference is significant.

**Table 8.** Derived Fe Abundances

| Star                  | [Fe I/H] ± $\sigma_{\text{stat.}}$ ± $\sigma_{\text{sys.}}$ (all lines)     | N <sub>Fe I</sub>  |
|-----------------------|---|--------------------|
|                       | [Fe I/H] ± $\sigma_{\text{stat.}}$ ± $\sigma_{\text{sys.}}$ (E.P. > 1.2 eV) | N <sub>Fe I</sub>  |
|                       | [Fe II/H] ± $\sigma_{\text{stat.}}$ ± $\sigma_{\text{sys.}}$                | N <sub>Fe II</sub> |
|                       | [Fe II/H] − [Fe I/H] ± $\sigma_{\text{stat.}}$ ± $\sigma_{\text{sys.}}$     |                    |
| BD+03°740             | −2.89 ± 0.01 ± 0.07   | 230                |
|                       | −2.91 ± 0.01 ± 0.06   | 100                |
|                       | −2.93 ± 0.02 ± 0.07   | 58                 |
|                       | −0.02 ± 0.02 ± 0.07   | ...                |
| BD−13°3442            | −2.84 ± 0.01 ± 0.09   | 243                |
|                       | −2.85 ± 0.01 ± 0.06   | 100                |
|                       | −2.85 ± 0.02 ± 0.08   | 63                 |
|                       | +0.00 ± 0.02 ± 0.07   | ...                |
| CD−33°1173            | −2.89 ± 0.01 ± 0.14   | 194                |
|                       | −2.98 ± 0.01 ± 0.10   | 61                 |
|                       | −3.07 ± 0.02 ± 0.07   | 55                 |
|                       | −0.10 ± 0.02 ± 0.08   | ...                |
| G 64-12               | −3.26 ± 0.02 ± 0.11   | 98                 |
|                       | −3.28 ± 0.02 ± 0.08   | 26                 |
|                       | −3.42 ± 0.02 ± 0.08   | 37                 |
|                       | −0.12 ± 0.02 ± 0.09   | ...                |
| HD 19445              | −2.14 ± 0.01 ± 0.08   | 261                |
|                       | −2.17 ± 0.01 ± 0.06   | 166                |
|                       | −2.20 ± 0.03 ± 0.07   | 36                 |
|                       | −0.03 ± 0.03 ± 0.06   | ...                |
| HD 84937 <sup>a</sup> | −2.24 ± 0.01 ± 0.10   | 260                |
|                       | −2.26 ± 0.01 ± 0.09   | 164                |
|                       | −2.23 ± 0.02 ± 0.07   | 27                 |
|                       | +0.03 ± 0.01 ± 0.07   | ...                |
| HD 94028              | −1.54 ± 0.01 ± 0.09   | 188                |
|                       | −1.56 ± 0.01 ± 0.08   | 139                |
|                       | −1.65 ± 0.03 ± 0.08   | 20                 |
|                       | −0.09 ± 0.03 ± 0.07   | ...                |

NOTE—The differences in the fourth line listed for each star reflect the [Fe I/H] ratios computed when lines with E.P. < 1.2 eV are excluded.

<sup>a</sup> Rederived; see Section 6.1

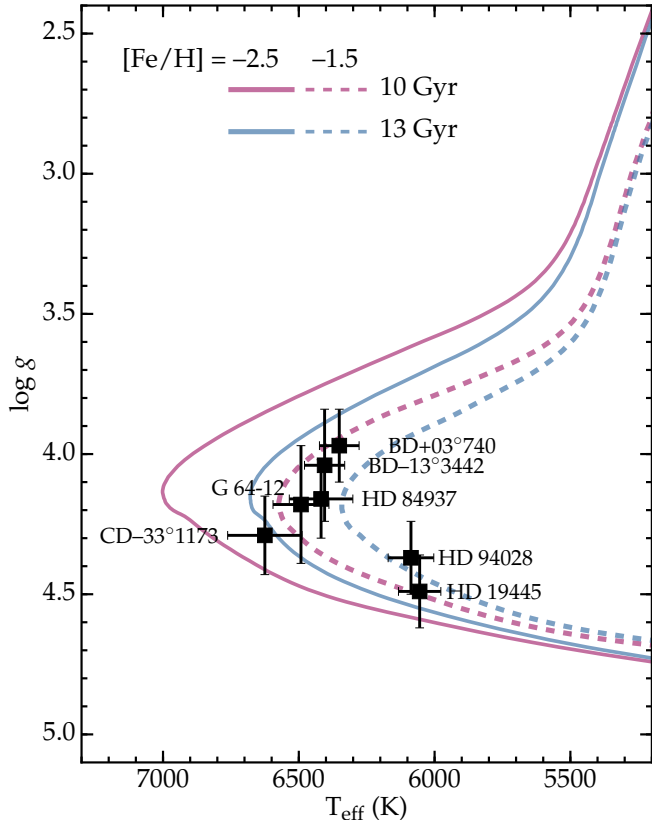


**Figure 2.** Comparison of our calculated  $T_{\text{eff}}$  and  $\log g$  with a set of Dartmouth isochrones (Dotter et al. 2008). The colors and line types distinguish the different ages and metallicities, which are indicated. The six stars in our sample, and our calculated values for HD 84937 (Section 6.1), are marked and labeled.

### 5.5. Comparisons between Abundances Derived from EWs and Spectrum Synthesis

Sneden et al. (2016) derived abundances in HD 84937 by spectrum synthesis, whereas we use EW-based abundances. To compare the two approaches, we measure EWs for the lines listed in Table 3 of Sneden et al. from the UVES spectra of HD 84937. We do not measure EWs for all of these lines because some minor blends are clearly visible. Adopting the same model atmosphere as Sneden et al. used for HD 84937, our EW measurements yield metallicities of  $-2.34 \pm 0.01$  (stat.)  $\pm 0.09$  (sys.) from 162 Fe I lines with E.P.  $> 1.2$  eV, and  $-2.32 \pm 0.02$  (stat.)  $\pm 0.10$  (sys.) from 27 Fe II lines. For the same subset of lines, the synthesis approach yields metallicities from Fe I and Fe II lines of  $-2.30 \pm 0.01$  (stat.)  $\pm 0.07$  (sys.) and  $-2.31 \pm 0.01$  (stat.)  $\pm 0.06$  (sys.), respectively. These values are identical to the abundances derived from the full set of Fe I and Fe II lines examined by Sneden et al.:  $-2.30 \pm 0.01$  ( $\sigma = 0.07$ , 446 lines) and  $-2.31 \pm 0.01$  ( $\sigma = 0.06$ , 105 lines), respectively.

We discussed in Sections 4.3 and 5.4 how the use of STIS E230M ( $R \sim 30,000$ ) spectra compared with higher resolution STIS E230H ( $R \sim 114,000$ ) spectra. We now extend that comparison to synthesis-based abundances derived from the E230M and E230H spectra. We create line lists by substituting laboratory  $\log gf$  values and hyperfine splitting structure line component patterns into the Kurucz (2011) line lists, and we synthesize these using MOOG. Figure 1 compares these synthetic spectra to the observed ones. Many of the lines are identified, and the strengths of most are fit reasonably well. Improved empirical and theoretical calculations (see, e.g., Peterson & Kurucz 2015; Peterson et al. 2017) and laboratory measurements (see, e.g., Lawler et al. 2017) are major contributors to this success. A fair number of observed features remain unidentified in our line lists (e.g., lines at 2492.24, 2496.06, and 2505.43 Å), and the oscillator strengths of other identified lines are still far from precise (e.g., lines at 2480.39, 2492.87, and 2498.70 Å). No  $\log gf$  values determined from modern laboratory work have been published for these lines to the best of our knowledge. We underscore that our goal in the present study is to analyze the abundances derived from a limited number of well-selected lines, not provide an exhaustive analysis of all UV features. Table 4 lists the lines with abundances derived by spectrum synthesis. The E230M spectrum and E230H spectrum of HD 84937 yield synthesis-based abundances different by  $-0.017 \pm 0.010$  dex ( $\sigma = 0.10$  dex, 93 lines), and the difference is  $-0.055 \pm 0.037$  dex ( $\sigma = 0.10$  dex, 8 lines) for HD 94028. Neither of these differences is significant.

Finally, we compare the EW-based and synthesis-based abundances derived from the E230H spectra of HD 84937 and HD 94028. These abundances are listed in Table 4. The difference (in the sense of EW-based abundance minus synthesis-based abundance) is  $+0.033 \pm 0.014$  dex ( $\sigma = 0.14$  dex, 93 lines) in HD 84937. The difference is  $-0.041 \pm 0.039$  dex ( $\sigma = 0.11$  dex, 8 lines) in HD 94028. Again, neither of these is significant.

Several points are worth mentioning. First, the differences between abundances derived from EW or synthesis are small ( $< 0.04$  dex), regardless of whether optical or UV spectra are considered. Second, the standard deviation increases slightly (by 0.02–0.04 dex) when using EWs when compared with synthesis, but the statistical errors on the mean remain small (0.01–0.02 dex) with both techniques. Third, the offset between the abundances derived from Fe I and Fe II lines is always 0.02 dex or less, regardless of whether EW-based or synthesis-based abundances are used. Fourth, HD 84937 and HD 94028 are two of the three most metal-rich stars in our sample, so any effects of blends are likely to be diminished in the more metal-poor stars. We conclude from these tests that it is acceptable to use EWs to derive Fe abundances from these Fe I and Fe II lines, and

the results are not substantially different from those derived by the spectrum synthesis method.

### 5.6. Other Potential Sources of Error

Other factors in the calculations could potentially affect the derived abundances. These include our choice of model atmosphere grid, Fe partition functions, Fe II  $\log gf$  values, and treatment of Rayleigh scattering in the blue and near-UV portions of the spectrum. We now quantify the impact of these decisions, and we conclude that none of these effects significantly affects our derived  $[\text{Fe}/\text{H}]$  ratios. We also investigate whether undetected binary companions could bias the photometry of these stars, thus impacting the stellar parameters we calculate.

#### 5.6.1. Choice of Model Atmosphere Grid

The MARCS grid of 1D, LTE, plane-parallel model atmospheres (Gustafsson et al. 2008) offers an alternative to the ATLAS9 grid. We interpolate a set of models from this grid with the same stellar parameters as given in Table 7, using an interpolation code provided by A. McWilliam (2009, private communication). We verify that the  $[\text{Fe}/\text{H}]$  ratios derived from either grid of models agree to better than 0.01 dex, so the choice of model atmosphere grid has no impact on our derived abundances.

#### 5.6.2. Fe Partition Functions

In principle, incomplete partition functions could introduce an offset between the  $[\text{Fe}/\text{H}]$  ratios derived from Fe I and Fe II lines. The standard 2017 version of MOOG uses interpolations of Fe I, II, and III partition functions from ATLAS9. The derived Fe abundances change by only  $-0.002$  dex if we instead adopt interpolations of these partition functions from the latest version (v. 5.5.1) of the NIST ASD. The only unobserved levels for Fe I or II are all high, and their effects on the partition functions will be  $\lesssim 1\%$ . The ATLAS9 partition functions for the species of interest are more than sufficient to compute Fe abundances to better than 0.01 dex precision.

#### 5.6.3. Fe II $\log gf$ values

Meléndez & Barbuy (2009) presented an alternative set of  $\log gf$  values for Fe II lines in the optical part of the spectrum ( $\lambda > 4087 \text{ \AA}$ ). There are only a few lines that overlap with those measured by us (3–13 lines per star). The Meléndez & Barbuy  $\log gf$  values are consistently smaller than the NIST  $\log gf$  values for these lines, leading to increases of 0.09 to 0.11 dex in the mean abundances derived from Fe II lines. We regard this as a potential systematic uncertainty in the  $[\text{Fe II}/\text{H}]$  zero-point. Most of the Fe II lines examined by us are at shorter wavelengths than those included in the Meléndez & Barbuy study, so we retain the NIST set of  $\log gf$  values.

#### 5.6.4. Treatment of Rayleigh Scattering

The continuous opacity is dominated by bound-free transitions of the  $\text{H}^-$  ion in the blue and UV portions of the spectrum in warm, metal-poor stellar atmospheres. The contributions from Rayleigh scattering become significant in cooler atmospheres, and incorrect treatment of this contribution can lead to overestimates of the abundances derived from lines in the blue and UV. Recent versions of MOOG have included the capability to calculate this contribution either as pure absorption (the traditional approach) or as isotropic, coherent scattering (Sobeck et al. 2011). We verify that both approaches give identical results, to better than 0.01 dex, in the mean  $[\text{Fe}/\text{H}]$  ratios derived for all of the stars in our sample. Thus the treatment of Rayleigh scattering in MOOG has no impact on our derived abundances.

#### 5.6.5. Undetected Binary Companions

The presence of undetected binary companions could bias the color- $T_{\text{eff}}$  calibrations by subtly altering the input photometry. We regard this possibility as unlikely because all six stars in our sample, and HD 84937, have been subjected to long-term radial velocity monitoring with precisions  $\approx 1 \text{ km s}^{-1}$  or better. These measurements span decades, yet no significant velocity variations have been detected in any of these seven stars (e.g., Smith et al. 1998; Ryan et al. 1999; Carney et al. 2001; Latham et al. 2002; Aoki et al. 2006; Asplund et al. 2006; Roederer et al. 2014). While the presence of face-on orbits or extremely long periods cannot be excluded, there is no evidence from velocities of binarity among the stars in our sample.

## 6. COMPARISON WITH OUR GROUP'S PREVIOUS STUDY OF HD 84937

We now recalculate the stellar parameters and re-derive the metallicity of HD 84937 using the methods described in Section 5 and compare with the results of Sneden et al. (2016). This comparison will help establish the reliability of our methods and place both studies on a single abundance scale.

### 6.1. Comparison of Stellar Parameters and Fe Abundances

We re-derive the stellar parameters of HD 84937 using the procedure described in Section 5. We find  $T_{\text{eff}} = 6418 \pm 117 \text{ K}$ ,  $\log g = 4.16 \pm 0.14$ ,  $v_t = 1.50 \pm 0.20 \text{ km s}^{-1}$ , and  $[\text{M}/\text{H}] = -2.25 \pm 0.10$ . For comparison, Sneden et al. (2016) adopted the parameters found by Lawler et al. (2013),  $T_{\text{eff}} = 6300 \pm 100 \text{ K}$ ,  $\log g = 4.0 \pm 0.2$ ,  $v_t = 1.50 \pm 0.25 \text{ km s}^{-1}$ , and  $[\text{M}/\text{H}] = -2.15 \pm 0.10$ . Using our model parameters, we derive  $[\text{Fe}/\text{H}] = -2.26 \pm 0.01 \text{ (stat.)} \pm 0.09 \text{ (sys.)}$  from 162 Fe I lines with E.P.  $> 1.2 \text{ eV}$  and  $[\text{Fe}/\text{H}] = -2.23 \pm 0.02 \text{ (stat.)} \pm 0.07 \text{ (sys.)}$  from 27 Fe II lines. There is a small metallicity offset between

the two analyses, mainly driven by the difference in  $T_{\text{eff}}$ . This difference will be minimal when considering the ratios of abundances of elements within the iron group, whose line strengths respond in similar ways to changes in the model atmosphere.

We place the [Snedden et al. \(2016\)](#) study of HD 84937 on the same metallicity scale as the present study by conducting a line-by-line differential analysis. The  $T_{\text{eff}}$ ,  $\log g$ , and  $[\text{Fe}/\text{H}]$  of HD 84937 are most similar to BD-13°3442, and a line-by-line differential analysis of 242 Fe I lines in HD 84937 and BD-13°3442 reveals that HD 84937 is  $0.53 \pm 0.01$  dex ( $\sigma = 0.11$  dex) more metal-rich than BD-13°3442. Thus, on our scale where BD-13°3442 is the reference, HD 84937 has a metallicity of  $-2.32$ .

## 6.2. External Comparison to the Gaia-ESO Survey

[Lawler et al. \(2013\)](#) assessed the agreement of derived stellar parameters for HD 84937 among previous studies in the literature. HD 84937 is the only star in our sample that is also a benchmark star for the *Gaia*-ESO Survey, so we now compare those results with our own. The  $T_{\text{eff}}$ ,  $\log g$ , and  $v_t$  values derived by us are in good agreement with those derived by [Jofré et al. \(2014\)](#) and [Heiter et al. \(2015\)](#):  $T_{\text{eff}} = 6356 \pm 97$  K,  $\log g = 4.06 \pm 0.04$ , and  $v_t = 1.39 \pm 0.24$  km s $^{-1}$ . The LTE  $[\text{Fe I}/\text{H}]$  ratio derived by [Jofré et al.](#),  $-2.09 \pm 0.08$ , is higher than our value by  $0.17 \pm 0.12$  dex. Using the *Gaia*-ESO Survey stellar parameters and our line list and EWs reduces the discrepancy by 0.04 dex. The *Gaia*-ESO Survey used only 20 Fe I lines with  $\lambda > 4900$  Å in HD 84937, and different  $\log gf$  values among the 10 lines in common can account for another 0.02 dex. Using lines only at redder wavelengths would also increase our derived  $[\text{Fe I}/\text{H}]$  ratio by 0.02 dex (Section 7.2). Together, these effects can reconcile our derived  $[\text{Fe I}/\text{H}]$  ratio for HD 84937 with that of the *Gaia*-ESO Survey.

## 7. DISCUSSION

### 7.1. Good Agreement between Abundances Derived from Fe I and Fe II Lines

The Fe abundances derived separately from Fe I and Fe II lines, listed in Table 8, are in good agreement with each other when strong lines and Fe I lines with E.P.  $< 1.2$  eV are excluded. The  $T_{\text{eff}}$  and  $\log g$  values are calculated largely independently from the spectra (Section 5), so the agreement between  $[\text{Fe I}/\text{H}]$  and  $[\text{Fe II}/\text{H}]$  is not preordained by construction. The offsets are small, with  $[\text{Fe II}/\text{H}] - [\text{Fe I}/\text{H}]$  ranging from  $-0.12$  dex to 0.00 dex. Using the [Meléndez & Barbuy \(2009\)](#)  $\log gf$  values for a small subset of optical Fe II lines (Section 5.6.3) would yield offsets in  $[\text{Fe II}/\text{H}] - [\text{Fe I}/\text{H}]$  of  $-0.02$  to  $+0.09$  dex. Systematic uncertainties that account for errors in the model atmosphere parameters and EW measurements are 0.07–0.09 dex, so neither set of offsets is highly significant.

The Fe I lines with E.P.  $< 1.2$  eV constitute a substantial fraction of all Fe I lines measured, ranging from 26% in the most metal-rich star to 73% in the most metal-poor star. The difference in  $[\text{Fe I}/\text{H}]$  when derived from all lines and only those with E.P.  $> 1.2$  eV is 0.03 dex or smaller in six of the seven stars, and the difference is 0.09 dex in CD-33°1173. This small difference may explain why some previous studies elected not to exclude low-E.P. Fe I lines (e.g., [Boesgaard et al. 2011](#)). One of the studies that recommended omitting the low-E.P. lines, [Lai et al. \(2008\)](#), found that the differences in abundances derived from the low-E.P. and high-E.P. Fe I lines were smallest in the stars with stellar parameters like those in our sample ( $T_{\text{eff}} > 6000$  K and  $[\text{Fe}/\text{H}] > -3.3$ ). That study found that the average slope between the derived abundance and the E.P. differed by  $-0.01$  dex eV $^{-1}$  when all Fe I lines were considered and when only Fe I lines with E.P.  $> 1.2$  eV were considered. We adopt the set of  $[\text{Fe}/\text{H}]$  ratios derived from Fe I lines with E.P.  $> 1.2$  eV because there is a systematic difference, however small. Had we chosen to retain the low-E.P. Fe I lines, our derived  $[\text{Fe}/\text{H}]$  ratios would be affected only minimally, and both sets of results are presented in Table 8.

Comparisons with the non-LTE corrections reported in the INSPECT database ([Bergemann et al. 2012](#); [Lind et al. 2012](#)) affirm this conclusion. The INSPECT web interface computes non-LTE corrections for specific Fe I or Fe II lines by interpolating a pre-computed grid for a given EW and stellar parameters. There are only 15–30 Fe I lines in common between the INSPECT database and ones measured for the different stars in our study, but the predicted non-LTE corrections are consistent for these lines. For each star, the non-LTE corrections for the two sets of Fe I lines (E.P.  $< 1.2$  eV, E.P.  $> 1.2$  eV) are always consistent to within 0.03 dex. These corrections range from  $+0.02$  dex for the most metal-rich stars to  $+0.13$  dex for the most metal-poor one. Subsequent work by [Amarsi et al. \(2016\)](#) also found consistent LTE and non-LTE offsets for these two sets of Fe I lines in their 1D models, as can be seen in their Figure 2.

Studies are in agreement that non-LTE corrections for  $[\text{Fe}/\text{H}]$  derived from Fe II lines are generally negligible,  $\lesssim 0.01$  dex ([Mashonkina et al. 2011](#); [Bergemann et al. 2012](#); [Lind et al. 2012](#); [Amarsi et al. 2016](#)). We verify this by checking individual Fe II lines in the stars in our sample with the non-LTE corrections reported in the INSPECT database, and the corrections are always  $< 0.01$  dex.

Our LTE  $[\text{Fe}/\text{H}]$  values are in reasonable agreement with other recent comparisons of LTE and non-LTE abundances in these warm, metal-poor dwarf stars. These studies have focused on lines available in the optical portion of the spectrum. [Mashonkina et al. \(2011\)](#) built a more complete model atom for Fe than had been available previously, and they derived  $[\text{Fe II}/\text{H}] - [\text{Fe I}/\text{H}] = +0.09 \pm 0.08$  in LTE for

HD 84937. When a wide range of non-LTE inelastic collision strengths with neutral hydrogen were considered, their non-LTE corrections to the  $[\text{Fe}/\text{H}]$  ratio derived from Fe I lines varied from +0.04 to +0.21 dex. These non-LTE values are not in significant conflict with our LTE results.

Bergemann et al. (2012) studied HD 84937 and G 64-12, and using MARCS models they found  $[\text{Fe II}/\text{H}] - [\text{Fe I}/\text{H}] = +0.01 \pm 0.10$  in LTE for HD 84937 and  $[\text{Fe II}/\text{H}] - [\text{Fe I}/\text{H}] = -0.02 \pm 0.10$  in LTE for G 64-12. Their non-LTE corrections to  $[\text{Fe}/\text{H}]$  derived from Fe I lines are 0.07 dex for HD 84937 and 0.11 dex for G 64-12. Both the LTE and non-LTE values are in fair agreement with our LTE results for these two stars.

Sitnova et al. (2015) derived  $[\text{Fe}/\text{H}]$  from both LTE and non-LTE calculations for 20 benchmark stars with reliable parallax measurements, including HD 84937 and HD 94028. For HD 84937 they found  $[\text{Fe II}/\text{H}] - [\text{Fe I}/\text{H}] = +0.06 \pm 0.11$  in LTE, and for HD 94028 they found  $[\text{Fe II}/\text{H}] - [\text{Fe I}/\text{H}] = +0.06 \pm 0.11$  in LTE. Their non-LTE corrections decreased these offsets by 0.06 and 0.02 dex, respectively. These results are also in fair agreement with our own.

Finally, Ezzeddine et al. (2017) predicted that the non-LTE corrections in G 64-12 and HD 84937 should be  $+0.29 \pm 0.10$  and  $+0.14 \pm 0.07$  dex, based on the extrapolation of a linear relationship they derived from stars with  $[\text{Fe}/\text{H}] \lesssim -4$  in LTE. The correction for G 64-12 is notably larger than would be expected based on our result, and the correction for HD 84937 is marginally larger. We notice that the Ezzeddine et al. linear relation changes if only the five stars with Fe detections and  $T_{\text{eff}} > 6000$  K are considered:  $\Delta[\text{Fe}/\text{H}] = -0.17 \times [\text{Fe}/\text{H}]_{\text{LTE}} - 0.33$ . This relation would predict corrections of +0.22 and +0.03 dex for G 64-12 and HD 84937, respectively, and the latter value is well within the range allowed by our results. We emphasize that the largest Fe I non-LTE corrections found by Ezzeddine et al. are predicted for stars with lower metallicities than those considered in the present study, and those stars are too faint for comparable UV observations with STIS.

### 7.2. Abundances Derived from Lines in the Balmer Dip Region

Figure 3 shows abundance trends as a function of wavelength. The Fe I lines between 3100 and 3700 Å have mildly (0.03–0.14 dex) lower abundances, on average, than lines at shorter or longer wavelengths. Table 9 lists these values. Roederer et al. (2012) noticed that Fe I lines in this wavelength range yielded abundances that were systematically lower by 0.16 to 0.27 dex than those at shorter or longer wavelengths in four metal-poor giants. Our study confirms a similar effect in the six dwarfs studied here, although the magnitude of the effect is substantially reduced. The data of Sneden et al. (2016) also reveal a reduction of 0.08 dex in the

abundances derived from Fe I lines with 3100–3700 Å in HD 84937, in agreement with the sign and magnitude of our results for other dwarf stars. Hereafter, we refer to this as the “Balmer Dip” effect, reflecting the fact that it affects lines near the convergence of the Balmer series and the beginning of the Balmer continuum wavelength region.

Curiously, the effect is reversed for some of the stars when Fe II lines are considered. Table 9 also lists these values. The number of Fe II lines in the 3100–3700 Å region is limited, however, to a handful of lines with wavelengths between 3167 and 3303 Å, so these lines are less informative than the Fe I lines, which span the full wavelength range. The analysis of Fe II within the discrepant wavelength range of HD 84937 is also restricted to this set of Fe II lines.

The Balmer Dip effect is not unique to the MOOG line analysis code. Similar results are clearly seen, for example, in Figure 6 of Ito et al. (2013), who found a systematic decrease of  $\approx 0.10$ – $0.15$  dex in abundances derived from Fe I lines in the Balmer Dip region in the metal-poor giant ( $T_{\text{eff}} = 5430$  K) BD+44°493. That study made use of a line analysis code derived from the work of Tsuji (1978). The analysis of the warm ( $T_{\text{eff}} = 6050$  K) dwarf star WISE J0725–2351 by Spite et al. (2015) using the Turbospectrum code (Alvarez & Plez 1998) reveals an abundance decrease of  $0.18 \pm 0.03$  dex when derived from Fe I lines inside the Balmer Dip region. We have not performed an exhaustive search for other studies that show similar effects, but these two examples demonstrate that the Balmer Dip effect is found in Fe abundances derived from multiple line analysis codes.

One possible cause of the Balmer Dip effect could be that lines in this wavelength range preferentially arise from electronic levels whose populations are overionized relative to their LTE values, leading to an underprediction of the abundances. If so, all lines arising from these levels should yield low abundances, whether or not the wavelengths are in the Balmer Dip region. Wood et al. (2013), who focused on Ti II, performed related tests for lines in HD 84937, and concluded that this was not the cause of the effect. In that study, Ti II lines arising from the more highly-excited levels ( $> 0.6$  eV) with wavelengths in the Balmer Dip region yielded low abundances, but lines at other wavelengths arising from these levels and lines inside and outside the Balmer Dip region arising from lower levels yielded consistent abundances.

Here, equipped with lines in six additional stars, we are in a better position to definitively test this hypothesis. For a given star, we identify levels that have at least three Fe I lines in the Balmer Dip region and at least three Fe I lines outside the Balmer Dip region. For each level, we compute the mean abundance derived from lines inside the Balmer Dip region and those outside the Balmer Dip region. We repeat this test for each of the six stars in our sample and HD 84937 from Sneden et al. (2016). A difference of zero would indicate that the

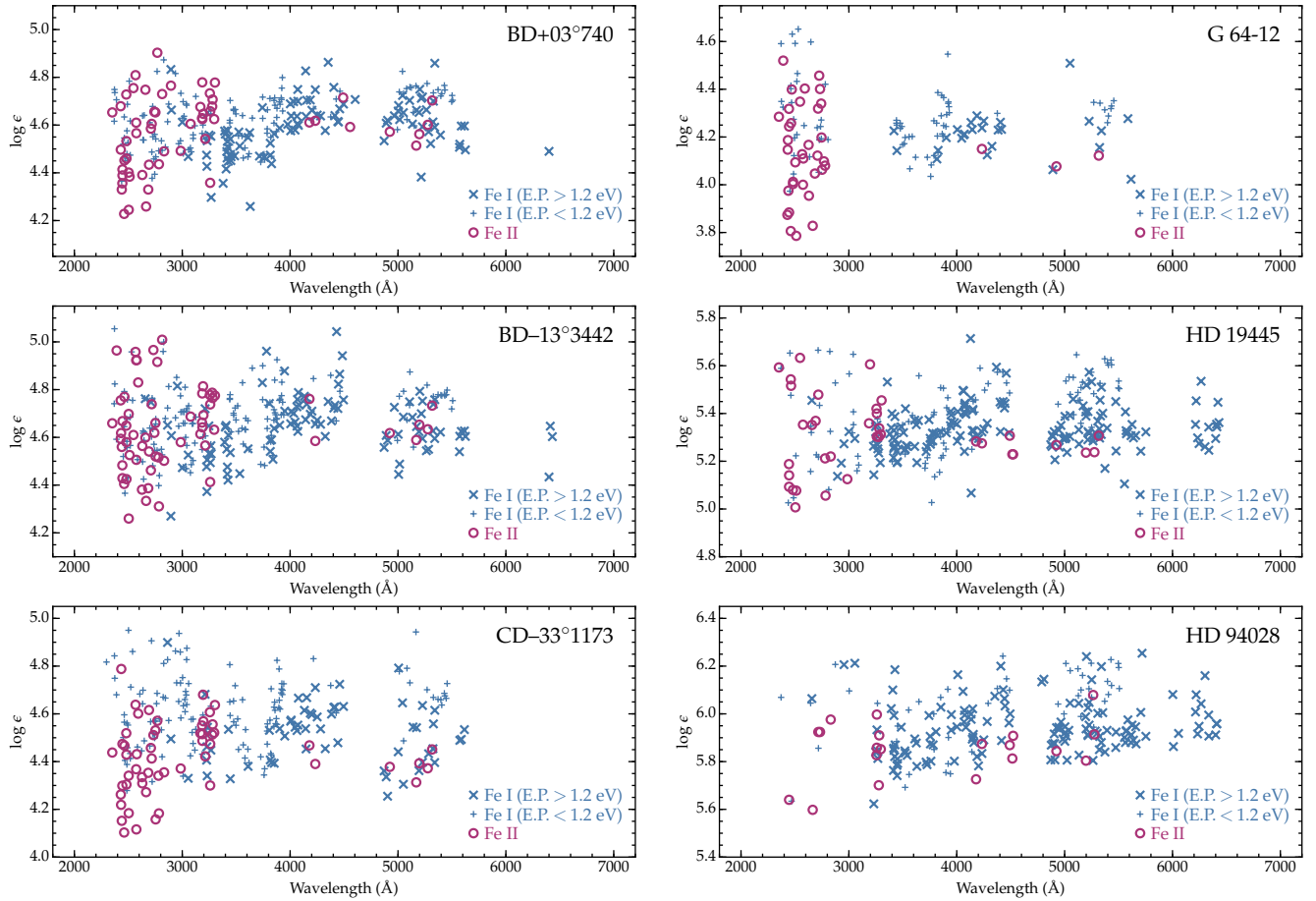


**Figure 3.** Derived Fe abundances versus wavelength for the six stars in our sample. The blue crosses and plus signs denote Fe I lines, and the red circles denote Fe II lines.

level populations themselves could be the source of the Balmer Dip effect. A non-zero difference would indicate that the levels are not the cause of the effect.

The results of this test are shown in Figure 4. There are 11 electronic levels of neutral Fe that meet our criteria, although not all levels meet these criteria for each of the seven stars considered. These levels are associated with multiplets from the  $3d^64s^2 a^5D$  ground state and the  $3d^7(4F)4s a^5F$ ,  $3d^64s^2 a^3P$ , and  $3d^7(4P)4s a^5P$  excited states. The mean abundance differences between Fe I lines outside the Balmer Dip region and Fe I lines inside the Balmer Dip region are usually positive and non-zero, and most are significant by several standard deviations. Two levels are each discrepant in one star ( $a^5F_5$  in BD-13°3442 and  $a^3P_2$  in HD 19445), but these levels only meet our criteria for inclusion in two stars, so we are reluctant to draw firm conclusions from them. The  $a^5F_4$  level only meets our criteria for inclusion in one star (HD 84937), so we also do not draw firm conclusions from it. Individual levels often give rise to measured lines at wavelengths shorter and longer than the Balmer Dip region, so the upper levels are not influ-

encing the results found here. The significant, non-zero differences for the remaining eight levels falsify our hypothesis that the LTE level populations in these particular electronic levels could be the source of the Balmer Dip effect.

Unfortunately, no levels of singly-ionized Fe meet our criteria in any star in the sample, so we cannot perform this test for Fe II lines.

The possibility that the Balmer Dip effect could be a consequence of systematic uncertainties in the branching fractions of upper transition levels has also been considered by Lawler & Den Hartog (2018). That study discussed several effects that could impact the calibration of branching ratios of Ar I and II in laboratory hollow cathode lamp spectra, which are commonly used to calibrate branching fractions of other species. Lawler & Den Hartog conclude that these calibration issues are not likely to be important in the Balmer Dip effect, but further tests are ongoing.

Previous studies of lines of other species have yielded a range of outcomes with regard to systematic decreases in abundances derived from lines in the Balmer Dip region.

**Table 9.** Fe Abundance Deviations in the 3100–3700 Å Region

| Star                        | $\lambda < 3100 \text{ \AA}, \lambda > 3700 \text{ \AA}$ |     | $3100 \leq \lambda \leq 3700 \text{ \AA}$ |    | $\Delta$         |
|-----------------------------|--|-----|---|----|------------------|
|                             | $\langle \log \epsilon \rangle$                          | N   | $\langle \log \epsilon \rangle$           | N  |                  |
| Abundances from Fe I lines  |  |     |   |    |                  |
| BD+03°740                   | $4.63 \pm 0.01$  | 72  | $4.49 \pm 0.02$                           | 28 | $+0.14 \pm 0.03$ |
| BD−13°3442                  | $4.67 \pm 0.02$  | 80  | $4.54 \pm 0.03$                           | 20 | $+0.13 \pm 0.03$ |
| CD−33°1173                  | $4.53 \pm 0.02$  | 51  | $4.46 \pm 0.04$                           | 10 | $+0.07 \pm 0.05$ |
| G 64-12                     | $4.21 \pm 0.03$  | 24  | $4.18 \pm 0.07$                           | 2  | $+0.03 \pm 0.07$ |
| HD 19445                    | $5.35 \pm 0.01$  | 129 | $5.29 \pm 0.02$                           | 37 | $+0.06 \pm 0.02$ |
| HD 84937 <sup>a</sup>       | $5.22 \pm 0.01$  | 367 | $5.14 \pm 0.01$                           | 79 | $+0.08 \pm 0.01$ |
| HD 94028                    | $5.96 \pm 0.01$  | 114 | $5.87 \pm 0.03$                           | 25 | $+0.09 \pm 0.03$ |
| Abundances from Fe II lines |  |     |   |    |                  |
| BD+03°740                   | $4.55 \pm 0.03$  | 45  | $4.65 \pm 0.04$                           | 13 | $-0.10 \pm 0.04$ |
| BD−13°3442                  | $4.63 \pm 0.03$  | 49  | $4.69 \pm 0.04$                           | 14 | $-0.06 \pm 0.05$ |
| CD−33°1173                  | $4.38 \pm 0.03$  | 41  | $4.52 \pm 0.03$                           | 14 | $-0.14 \pm 0.04$ |
| G 64-12                     | $4.14 \pm 0.03$  | 37  | ...                                       | 0  | ...              |
| HD 19445                    | $5.27 \pm 0.03$  | 27  | $5.39 \pm 0.04$                           | 9  | $-0.12 \pm 0.05$ |
| HD 84937 <sup>a</sup>       | $5.19 \pm 0.01$  | 91  | $5.22 \pm 0.01$                           | 14 | $-0.03 \pm 0.01$ |
| HD 94028                    | $5.85 \pm 0.04$  | 14  | $5.86 \pm 0.05$                           | 6  | $-0.01 \pm 0.06$ |

<sup>a</sup> Using abundances presented in [Snedén et al. \(2016\)](#)

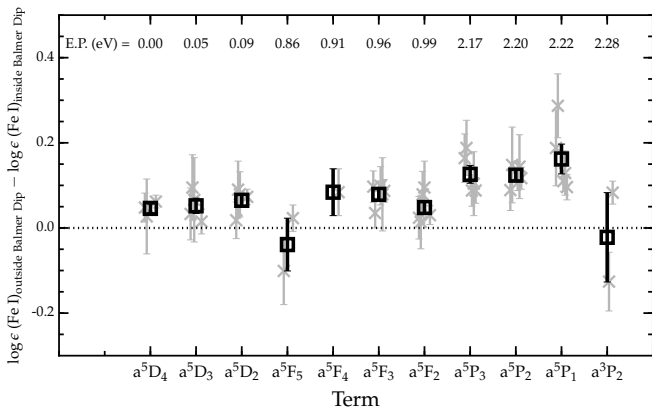


**Figure 4.** Mean abundance differences derived from Fe I lines outside and inside the Balmer Dip region ( $3100 \leq \lambda \leq 3700 \text{ \AA}$ ). The gray crosses—offset horizontally slightly for clarity—indicate the measurements from individual stars, where the number of lines per level ranges from 9 to 37, with a median of 15 lines. The gray error bars indicate the standard error on the difference. The black squares indicate the mean differences for a given level, and the black error bars indicate the standard error on this difference. The term designations are listed along the bottom, and the excitation potentials are listed along the top. The dotted line indicates zero difference.

Lines of Ti I, Ti II, and possibly V II show the effect in HD 84937 ([Lawler et al. 2013, 2014](#); [Wood et al. 2013, 2014b](#)). Lines of Sc II, Cr II, Co I, and Ni I do not show any discrepancy in HD 84937 ([Wood et al. 2014a](#); [Lawler et al. 2015](#); [Snedén et al. 2016](#)). Lines of V I,

Cr I, Mn I, and Mn II yield inconclusive results, because the number of lines available in the affected wavelength region of HD 84937 is small ([Lawler et al. 2014](#); [Snedén et al. 2016](#)). These results suggest that, at least in analyses of HD 84937, missing or incorrect treatment of the continuous opacity in the Balmer Dip region cannot be a major factor in the Balmer Dip effect. [Lawler et al. \(2013\)](#) and [Wood et al. \(2013\)](#) suggested that non-LTE effects in the H I  $n = 2$  level may be (partially) responsible. If so, then a closer comparison of the sets of species that are affected and the sets of species that are not affected may be key to diagnosing the line-forming layers of the atmosphere where the effect originates. As such, the Balmer Dip effect may be a useful and readily accessible tool to better understand 3D convection effects in the atmospheres of distant stars. Further investigation of this matter with the full set of iron-group abundances in our sample of six stars may offer new insight here.

## 8. CONCLUSIONS

We have collected new and archival high-resolution UV and optical spectra of six warm, metal-poor dwarf stars. Using stellar parameters calculated largely independent of the spectra themselves, we have derived [Fe/H] ratios from several hundred Fe I and Fe II lines with wavelengths between 2290 and 6430 Å. The Fe II lines should be adequately modeled using standard LTE assumptions, whereas Fe I may not. The [Fe/H] ratios derived separately from the two species are in agreement with each other to within  $\approx 1.3$  times their uncertainties when strong lines and Fe I lines with E.P.  $< 1.2$  eV are excluded. These results constrain the limits of departures from LTE to be minimal, at most, within the range of stellar parameters considered, for the higher-

excitation lines. This is in agreement with modern studies of non-LTE line formation in stars like these. Theoretical calculations of Fe I lines in non-LTE predict that the departures from LTE should increase substantially at metallicities lower than those examined by our study (e.g., [Ezzeddine et al. 2017](#)), so our results may not be generalizable to lower-metallicity dwarfs.

We have attempted to identify possible sources of error in our method and calculations, including the choice of 1D LTE plane-parallel model atmosphere grids, Fe partition functions, and the treatment of Rayleigh scattering in MOOG. None of these affect our derived [Fe/H] ratios in excess of 0.01 dex. A yet-unidentified source of uncertainty affects some abundances derived from lines in the wavelength region from approximately 3100 to 3700 Å, as has been found previously (cf., e.g., [Roederer et al. 2012](#)). Our investigations indicate that this Balmer Dip effect cannot be attributed exclusively to missing continuous opacity or non-LTE effects in several Fe I electronic levels that give rise to lines in this wavelength region. An analysis of the impact of the Balmer Dip effect on additional iron-group species may help to resolve the matter.

We thank the referee for suggesting several tests that have helped to strengthen the conclusions of this work. IUR also thanks A. Ji for useful conversations about MOOG. Generous support for Program GO-14232 has been provided by a grant from STScI, which is operated by AURA, under NASA contract NAS5-26555.

We also acknowledge partial support from National Science Foundation (NSF) grants PHY 14-30152 (Physics Frontier Center/JINA-CEE) and AST 16-16040 (to CS). This research has made use of NASA’s Astrophysics Data System Bibliographic Services; the arXiv pre-print server operated by Cornell University; the SIMBAD and VizieR database hosted by the Strasbourg Astronomical Data Center; the Atomic Spectra Database hosted by the National Institute of Standards and Technology; the MAST at STScI; the INSPECT database (v. 1.0; <http://www.inspect-stars.com>); and the IRAF software packages distributed by the National Optical Astronomy Observatories, which are operated by AURA, under cooperative agreement with the NSF. This work has also made use of data from the European Space Agency (ESA) mission *Gaia*, (<http://www.cosmos.esa.int/gaia>), processed by the *Gaia* Data Processing and Analysis Consortium (DPAC). <http://www.cosmos.esa.int/web/gaia/dpac/consortium>). Funding for the DPAC has been provided by national institutions, in particular the institutions participating in the *Gaia* Multilateral Agreement.

*Facility:* HST (STIS), Keck I (HIRES), Smith (Tull), VLT (UVES)

*Software:* IRAF ([Tody 1993](#)), MARCS ([Gustafsson et al. 2008](#)), matplotlib ([Hunter 2007](#)), MOOG ([Snedden 1973](#); [Sobeck et al. 2011](#), 2017 version), numpy ([van der Walt et al. 2011](#)), R ([R Core Team 2014](#)), scipy ([Jones et al. 2001](#))

## REFERENCES

- Alonso, A., Arribas, S., & Martínez-Roger, C. 1999, *A&AS*, 140, 261
- Alvarez, R., & Plez, B. 1998, *A&A*, 330, 1109
- Alves-Brito, A., Meléndez, J., Asplund, M., Ramírez, I., & Yong, D. 2010, *A&A*, 513, A35
- Amarsi, A. M., Lind, K., Asplund, M., Barklem, P. S., & Collet, R. 2016, *MNRAS*, 463, 1518
- Aoki, W., Frebel, A., Christlieb, N., et al. 2006, *ApJ*, 639, 897
- Asplund, M., Lambert, D. L., Nissen, P. E., Primas, F., & Smith, V. V. 2006, *ApJ*, 644, 229
- Asplund, M., Grevesse, N., Sauval, A. J., & Scott, P. 2009, *ARA&A*, 47, 481
- Barklem, P. S., Piskunov, N., & O’Mara, B. J. 2000, *A&AS*, 142, 467
- Barklem, P. S., & Asplund-Johansson, J. 2005, *A&A*, 435, 373
- Bergemann, M., Lind, K., Collet, R., Magic, Z., & Asplund, M. 2012, *MNRAS*, 427, 27
- Bergeson, S. D., Mullman, K. L., Wickliffe, W. E., et al. 1996, *ApJ*, 464, 1044
- Boesgaard, A. M., Rich, J. A., Levesque, E. M., & Bowler, B. P. 2011, *ApJ*, 743, 140
- Bohlin, R. C., Savage, B. D., & Drake, J. F. 1978, *ApJ*, 224, 132
- Bonifacio, P., Monai, S., & Beers, T. C. 2000, *AJ*, 120, 2065
- Bressan, A., Marigo, P., Girardi, L., et al. 2012, *MNRAS*, 427, 127
- Carney, B. W., Latham, D. W., Laird, J. B., Grant, C. E., & Morse, J. A. 2001, *AJ*, 122, 3419
- Carretta, E., Gratton, R., Cohen, J. G., Beers, T. C., & Christlieb, N. 2002, *AJ*, 124, 481
- Casagrande, L., Ramírez, I., Meléndez, J., Bessell, M., & Asplund, M. 2010, *A&A*, 512, A54
- Casagrande, L., Schönrich, R., Asplund, M., et al. 2011, *A&A*, 530, A138
- Casagrande, L., & Vandenberg, D. A. 2014, *MNRAS*, 444, 392
- Castelli, F., Kurucz, R. L. *Proc. IAU Symp. No 210, Modelling of Stellar Atmospheres*, N. Piskunov et al., eds. 2003, A20

- Cayrel, R., Depagne, E., Spite, M., et al. 2004, *A&A*, 416, 1117
- Cohen, J. G., Christlieb, N., McWilliam, A., et al. 2008, *ApJ*, 672, 320-341
- Cohen, J. G., Christlieb, N., Thompson, I., et al. 2013, *ApJ*, 778, 56
- Collet, R., Asplund, M., & Thévenin, F. 2005, *A&A*, 442, 643
- Cutri, R. M., Skrutskie, M. F., van Dyk, S., et al. 2003, *VizieR Online Data Catalog: 2MASS All-Sky Catalog of Point Sources*, 2246, 0
- Dekker, H., D’Odorico, S., Kaufer, A., Delabre, B., & Kotzlowski, H. 2000, *Proc. SPIE*, 4008, 534
- Den Hartog, E. A., Ruffoni, M. P., Lawler, J. E., et al. 2014, *ApJS*, 215, 23
- Dotter, A., Chaboyer, B., Jevremović, D., et al. 2008, *ApJS*, 178, 89-101
- Ducati, J. R. 2002, *VizieR Online Data Catalog: Catalogue of Stellar Photometry in Johnson’s 11-color System*, 2237, 0
- Ezzeddine, R., Frebel, A., & Plez, B. 2017, *ApJ*, 847, 142
- Ferlet, R., Vidal-Madjar, A., & Gry, C. 1985, *ApJ*, 298, 838
- Fulbright, J. P. 2000, *AJ*, 120, 1841
- Gaia Collaboration, Brown, A. G. A., Vallenari, A., et al. 2016 (arXiv:1609.04172)
- Gustafsson, B., Edvardsson, B., Eriksson, K., et al. 2008, *A&A*, 486, 951
- Hansen, C. J., Primas, F., Hartman, H., et al. 2012, *A&A*, 545, A31
- Heiter, U., Jofré, P., Gustafsson, B., et al. 2015, *A&A*, 582, A49
- Hosford, A., Ryan, S. G., García Pérez, A. E., Norris, J. E., & Olive, K. A. 2009, *A&A*, 493, 601
- Hunter, J.D. 2011, *Computing in Science & Engineering*, 9, 90
- Ito, H., Aoki, W., Beers, T. C., et al. 2013, *ApJ*, 773, 33
- Ivans, I. I., Sneden, C., James, C. R., et al. 2003, *ApJ*, 592, 906
- Jofré, P., Heiter, U., Soubiran, C., et al. 2014, *A&A*, 564, A133
- Jones, E., Oliphant, E., Peterson, P., et al. 2001, *SciPy: Open Source Scientific Tools for Python*, <http://www.scipy.org>
- Kimble, R. A., Woodgate, B. E., Bowers, C. W., et al. 1998, *ApJL*, 492, L83
- Korn, A. J., Shi, J., & Gehren, T. 2003, *A&A*, 407, 691
- Kramida, A., Ralchenko, Y., Reader, J., and the NIST ASD Team. 2017, *NIST Atomic Spectra Database (v. 5.5.1)*, online, URL: <http://physics.nist.gov/asd>
- Kurucz, R. L. 2011, *Canadian Journal of Physics*, 89, 417
- Lai, D. K., Bolte, M., Johnson, J. A., et al. 2008, *ApJ*, 681, 1524-1556
- Latham, D. W., Stefanik, R. P., Torres, G., et al. 2002, *AJ*, 124, 1144
- Lawler, J. E., & Den Hartog, E. A. 2018, *JQSRT*, in press
- Lawler, J. E., Guzman, A., Wood, M. P., Sneden, C., & Cowan, J. J. 2013, *ApJS*, 205, 11
- Lawler, J. E., Wood, M. P., Den Hartog, E. A., et al. 2014, *ApJS*, 215, 20
- Lawler, J. E., Sneden, C., & Cowan, J. J. 2015, *ApJS*, 220, 13
- Lawler, J. E., Sneden, C., Cowan, J. J., Den Hartog, E. A., & Wood, M. P. 2017, *Canadian Journal of Physics*, 95, 783
- Lind, K., Bergemann, M., & Asplund, M. 2012, *MNRAS*, 427, 50
- Marigo, P., Girardi, L., Bressan, A., et al. 2017, *ApJ*, 835, 77
- Mashonkina, L., Gehren, T., Shi, J.-R., Korn, A. J., & Grupp, F. 2011, *A&A*, 528, A87
- McCall, M. L. 2004, *AJ*, 128, 2144
- Meléndez, J., & Barbuy, B. 2009, *A&A*, 497, 611
- Meléndez, J., Casagrande, L., Ramírez, I., Asplund, M., & Schuster, W. J. 2010, *A&A*, 515, L3
- Munari, U., Henden, A., Frigo, A., et al. 2014, *AJ*, 148, 81
- Nomoto, K., Kobayashi, C., & Tominaga, N. 2013, *ARA&A*, 51, 457
- O’Brian, T. R., Wickliffe, M. E., Lawler, J. E., Whaling, W., & Brault, J. W. 1991, *Journal of the Optical Society of America B Optical Physics*, 8, 1185
- Paunzen, E. 2015, *A&A*, 580, A23
- Peterson, R. C., Dorman, B., & Rood, R. T. 2001, *ApJ*, 559, 372
- Peterson, R. C., & Kurucz, R. L. 2015, *ApJS*, 216, 1
- Peterson, R. C., Kurucz, R. L., & Ayres, T. R. 2017, *ApJS*, 229, 23
- Pickering, J. C., Johansson, S., & Smith, P. L. 2001, *A&A*, 377, 361
- Pickering, J. C., Donnelly, M. P., Nilsson, H., Hibbert, A., & Johansson, S. 2002, *A&A*, 396, 715
- R Core Team, 2014, “R: A Language and Environment for Statistical Computing,” R Foundation for Statistical Computing, Vienna, Austria. URL <http://www.R-project.org>
- Ramírez, I., & Meléndez, J. 2005, *ApJ*, 626, 465
- Recio-Blanco, A., Piotto, G., Aparicio, A., & Renzini, A. 2002, *ApJL*, 572, L71
- Reggiani, H., Meléndez, J., Kobayashi, C., Karakas, A., & Placco, V. 2017, *A&A*, 608, A46
- Rich, J. A., & Boesgaard, A. M. 2009, *ApJ*, 701, 1519

- Roederer, I. U., Lawler, J. E., Sobek, J. S., et al. 2012, *ApJS*, 203, 27
- Roederer, I. U., Preston, G. W., Thompson, I. B., et al. 2014, *AJ*, 147, 136
- Ruffoni, M. P., Den Hartog, E. A., Lawler, J. E., et al. 2014, *MNRAS*, 441, 3127
- Ryan, S. G., Norris, J. E., & Beers, T. C. 1999, *ApJ*, 523, 654
- Schlafly, E. F., & Finkbeiner, D. P. 2011, *ApJ*, 737, 103
- Schlegel, D. J., Finkbeiner, D. P., & Davis, M. 1998, *ApJ*, 500, 525
- Schnabel, R., Schultz-Johanning, M., & Kock, M. 2004, *A&A*, 414, 1169
- Sikström, C. M., Schultz-Johanning, M., Kock, M., et al. 1999, *Journal of Physics B Atomic Molecular Physics*, 32, 5687
- Sitnova, T., Zhao, G., Mashonkina, L., et al. 2015, *ApJ*, 808, 148
- Smith, V. V., Lambert, D. L., & Nissen, P. E. 1998, *ApJ*, 506, 405
- Sneden, C.A. 1973, Ph.D. thesis, University of Texas at Austin
- Sneden, C., Cowan, J. J., Kobayashi, C., et al. 2016, *ApJ*, 817, 53
- Sobek, J. S., Kraft, R. P., Sneden, C., et al. 2011, *AJ*, 141, 175
- Spite, M., Spite, F., Caffau, E., & Bonifacio, P. 2015, *A&A*, 582, A74
- Spitzer, L. "Diffuse matter in space." 1968, New York: Interscience Publication, 1968,
- Thévenin, F., & Idiart, T. P. 1999, *ApJ*, 521, 753
- Tody, D. 1993, *Astronomical Data Analysis Software and Systems II*, 52, 173
- Tsuji, T. 1978, *A&A*, 62, 29
- Tull, R. G., MacQueen, P. J., Sneden, C., & Lambert, D. L. 1995, *PASP*, 107, 251
- Unsöld, A., *Physik der Sternatmosphären*, Springer-Verlag, Berlin, 1955, p. 332
- van der Walt, S., Colbert, S. C., Varoquaux, G. 2011, *Computing in Science & Engineering*, 13, 22
- van Leeuwen, F. 2007, *A&A*, 474, 653
- VandenBerg, D. A., Bond, H. E., Nelan, E. P., et al. 2014, *ApJ*, 792, 110
- Vogt, S. S., Allen, S. L., Bigelow, B. C., et al. 1994, *Proc. SPIE*, 2198, 362
- Wood, M. P., Lawler, J. E., Sneden, C., & Cowan, J. J. 2013, *ApJS*, 208, 27
- Wood, M. P., Lawler, J. E., Sneden, C., & Cowan, J. J. 2014, *ApJS*, 211, 20
- Wood, M. P., Lawler, J. E., Den Hartog, E. A., Sneden, C., & Cowan, J. J. 2014, *ApJS*, 214, 18
- Woodgate, B. E., Kimble, R. A., Bowers, C. W., et al. 1998, *PASP*, 110, 1183